



Geostationary observations of atmospheric ammonia over East Asia:

spatio-temporal variations revealed by three years of FY-4B/GIIRS

measurements 3

- Mengya Sheng¹, Runyi Zhou¹, Jiancong Hua¹, Shan Han¹, Shangyi Liu¹, Lin Zhang², Wei Wang³, Ruijun
- 5
- Dang⁴, Hansen Cao⁵, Zichong Chen⁶, Yixuan Gu⁷, Mingxu Liu⁸, Lu Lee⁹, Chengli Qi⁹, Feng Lu⁹, Changpei Han¹⁰, Mark W. Shephard¹¹, Nadir Guendouz¹², Camille Viatte¹², Lieven Clarisse¹³, Martin Van Damme^{13,14}, Cathy Clerbaux^{12,13}, Zhao-Cheng Zeng¹,* 6
- 7
- 8 ¹ School of Earth and Space Sciences, Peking University, Beijing 100871, China
- 9 ² Laboratory for Climate and Ocean-Atmosphere Studies, Department of Atmospheric and Oceanic Sciences, School of Physics,
- 10 Peking University, Beijing 100871, China
- 11 ³ Key Laboratory of Environmental Optics and Technology, Anhui Institute of Optics and Fine Mechanics, Chinese Academy
- 12 of Sciences, Hefei 230031, China
- 13 ⁴ School of Engineering and Applied Sciences, Harvard University, Cambridge, MA 02138, USA
- 14 ⁵ School of Environmental Science and Engineering, Southern University of Science and Technology, Shenzhen, Guangdong 15 518055, China
- ⁶ Hong Kong University of Science and Technology, Guangzhou 511400, China 16
- 17 ⁷ Jiangsu Key Laboratory of Atmospheric Environment Monitoring and Pollution Control, Collaborative Innovation Center of
- 18 Atmospheric Environment and Equipment Technology, Joint International Research Laboratory of Climate and Environment
- 19 Change, School of Environmental Science and Engineering, Nanjing University of Information Science and Technology,
- 20 Nanjing 210044, China
- 21 ⁸ College of Environmental Sciences and Engineering, Peking University, Beijing 100871, China
- 22 23 ⁹ Key Laboratory of Radiometric Calibration and Validation for Environmental Satellites, National Satellite Meteorological Center, China Meteorological Administration, Beijing 100081, China
- 24 ¹⁰Key Laboratory of Infrared Science and Technology, Shanghai Institute of Technical Physics, Chinese Academy of Sciences,
- 25 Shanghai 200083, China
- 26 ¹¹ Environment and Climate Change Canada, Toronto, Ontario M3H 5T4, Canada
- 27 ¹² LATMOS/IPSL, Sorbonne Université, UVSQ, CNRS, Paris 75252, France
- 28 ¹³ Spectroscopy, Quantum Chemistry and Atmospheric Remote Sensing (SQUARES), Brussels Laboratory of the Universe
- <u>2</u>9 (BLU-ULB), Université libre de Bruxelles (ULB), Brussels 1050, Belgium
- 30 ¹⁴ Royal Belgian Institute for Space Aeronomy, Brussels 1180, Belgium
- 31 Correspondence to: Zhao-Cheng Zeng (zczeng@pku.edu.cn)
- 32 **Abstract.** Satellite observations play a crucial role in quantifying ammonia sources by capturing large-scale variations of
- 33 atmospheric NH₃ concentrations. As the world's first geostationary hyperspectral infrared sounder, the Geostationary
- 34 Interferometric Infrared Sounder (GIIRS) on board China's FengYun-4 satellite series provides a unique opportunity to
- 35 monitor the diurnal cycle of NH₃. Using NH₃ retrievals between July 2022 and June 2025, this study investigates the spatio-
- 36 temporal variability of NH₃ columns over East Asia, with a focus on daytime variations (07:00–19:00 local time) in major
- 37 agricultural regions. Inter-comparison with polar-orbiting IASI and CrIS data shows that GIIRS NH3 retrievals are consistent
- 38 in capturing the spatial patterns and temporal dynamics. The NH₃ peaks occur between March and July, with the timing shifting





from north to south, reflecting regional differences primarily driven by agriculture activities. Validation with ground-based FTIR measurements at Hefei in eastern China demonstrates the accuracy of GIIRS NH₃, with a correlation coefficient of 0.77 and an RMSE of 9.67×10¹⁵ molec/cm², while reproducing daytime variations observed by FTIR. For major agricultural areas, the NH₃ columns generally increase from early morning to late afternoon, reaching 1.10–1.56 times morning levels in summer and spring. Compared with GEOS-CF model simulations, the results reveal pronounced discrepancies in spatial distributions over the Sichuan Basin in southwestern China and daytime variations over northern India. These findings highlight the valuable capability of FY-4B/GIIRS in identifying and tracking daytime dynamics of NH₃ sources over East Asia, offering new insights beyond current low-Earth orbit (LEO) instruments.

1 Introduction

Gaseous ammonia (NH₃), the most abundant alkaline gas and a major reactive nitrogen compound in the atmosphere, plays a critical role in the global nitrogen cycle. NH₃ is an important precursor of secondary inorganic aerosols. It rapidly reacts with atmospheric acids such as sulfuric acid (H₂SO₄) and nitric acid (HNO₃) to form ammonium sulfate ((NH₄)₂SO₄) and ammonium nitrate (NH₄NO₃) (Seinfeld et al., 2016). These ammonium-containing aerosols are the primary components of fine particulate matter (PM_{2.5}) and have been identified as key contributors to elevated PM_{2.5} concentrations and haze pollution in both rural areas (Jang et al., 2025; Saraswati et al., 2019; Meng Z. et al., 2018) and megacities (Lin et al., 2020) in Asia, posing significant threats to air quality, visibility, and public health. Through aerosol-mediated processes, NH₃ also indirectly influences the formation and removal of greenhouse gases such as nitrous oxide (N₂O) and methane (CH₄) by altering the oxidative capacity of the atmosphere (Pai et al., 2021). Moreover, excessive emissions and deposition of NH₃ have adverse effects on ecosystems, causing biodiversity loss, soil acidification, and water eutrophication (Bobbink et al., 2010). Anthropogenic NH₃ emissions primarily originate from agricultural activities, particularly from synthetic fertilizer application and livestock farming, with additional contributions from industrial processes and transportation (Behera et al., 2013). Numerous studies have indicated that a relatively strong reduction in PM_{2.5} and N₂O levels can be achieved by decreasing agricultural emissions (e.g., Luo et al., 2025). Therefore, comprehensive quantification and understanding of NH₃ emission sources are essential for developing effective air quality and climate mitigation strategies.

Asia is the world's most significant NH₃ emission hot spots, accounting for over 30% of global NH₃ emissions annually as reported by the EDGAR emission inventory. Due to widespread use of urea-based nitrogen fertilizers and high livestock densities, cropland areas such as the Indo-Gangetic Plain in India and the North China Plain in China are recognized as major global NH₃ emission hot spots (Van Damme et al., 2018). NH₃ volatilization is strongly controlled by surface conditions, including temperature and moisture, and irrigation-driven NH₄⁺ accumulation in soils (Behera et al., 2013). The resulting atmospheric NH₃ concentrations over a region are further influenced by meteorology- and topography-induced constraints on atmospheric mixing and transport, chemical reactions dependent on the concentrations of reactive acidic gases, and dry and wet deposition (Dammers et al., 2017a). In most regions, NH₃ concentration levels in summer are significantly higher than





those in winter, driven by emissions from urea hydrolysis and livestock manure decomposition (Warner et al., 2016; Van Damme et al., 2015). However, NH₃ has a short atmospheric lifetime of a few hours to several days, resulting in large intraday variability in concentrations from both agricultural and non-agricultural sources. Previous studies in Asia have primarily addressed the quantification of agricultural and non-agricultural sources using the bottom-up emission inventories and ground-based measurements, as well as the estimation of anthropogenic emissions inferred from NH₃ observations. Only a few studies have employed surface measurements to investigate the diurnal variability of NH₃ and its controlling mechanisms, and found that diurnal pattern of NH₃ variations in various urban and rural areas differ markedly across seasons (Chang et al., 2019; Huy et al., 2017; Meng Z. et al., 2011). Limited by the sparse spatial coverage and short temporal duration of ground-based monitoring networks, the mechanisms underlying the diurnal variation characteristics of atmospheric NH₃ in different emission source regions still remain poorly understood (Gu et al., 2022; He et al., 2020).

Satellite observations facilitate a top-down inversion method for monitoring NH₃ variations across different spatial scales. The hyperspectral infrared sounders onboard polar-orbiting satellites in low-Earth orbit (LEO), such as the Infrared Atmospheric Sounding Interferometer (IASI; Clarisse et al., 2009), the Tropospheric Emission Spectrometer (TES; Beer et al., 2008), the Atmospheric Infrared Sounder (AIRS; Warner et al., 2016), and the Cross-track Infrared Sounder (CrIS; Shephard et al., 2020), have provided global monitoring of atmospheric NH₃ column densities. Satellite-based NH₃ retrievals have been widely used to investigate the spatial distribution of NH₃ emission sources (e.g., Van Damme et al., 2018), to characterize spatiotemporal variations in atmospheric NH₃ concentrations (e.g., Van Damme et al., 2021; Shephard et al., 2020), and to constrain emission estimates (e.g., Cao et al., 2020; Dammers et al., 2019) and dry deposition estimates (e.g., Kharol et al., 2018). Van Damme et al. (2021) reported that NH₃ concentrations increased from 2008–2018 in major agricultural regions globally, including South Asia, China, the United States and some parts of Europe. Using multi-year NH₃ maps, Van Damme et al. (2018) and Clarisse et al. (2019) identified and quantified major industrial and agricultural NH₃ point sources, revealing that NH₃ emissions from approximately two-thirds of these sources were underestimated by at least one order of magnitude in the Emissions Database for Global Atmospheric Research (EDGAR) inventory. In addition, NH₃ emission estimates based on satellite observations and inverse modeling indicated that the bottom-up emission inventories underestimate NH₃ emissions, especially during summer (e.g., Xu et al., 2023; Marais et al., 2021; Zhang et al., 2018).

Accurately monitoring daily dynamics of NH₃ emissions imposes high sampling requirements in time and space on atmospheric NH₃ measurements. Polar-orbiting satellites typically measure a given location at most twice per day. For example, IASI and CrIS cross the equator at 09:30/21:30, and 01:30/13:30 local solar time (LST), respectively (Whitburn et al., 2016; Shephard et al., 2015). The above satellite-based studies mostly used morning observations from IASI and afternoon observations from CrIS, because of the lower uncertainties associated with a more favorable thermal state of the atmosphere for the remote sensing of its lowest layers. Investigations of the spatial and temporal variability of NH₃ are constrained by the limited coverage of satellite overpasses, leading to potential temporal representativeness biases and substantial uncertainties in daily NH₃ emission estimates (Clarisse et al., 2019; Van Damme et al., 2018). The Geostationary Interferometric Infrared Sounder (GIIRS) onboard the FY-4 series, the world's first hyperspectral infrared sounder in geostationary (GEO) orbit, was





first launched as an experimental instrument on FY-4A in 2016 and later upgraded to an operational version with enhanced sensitivity on FY-4B in 2021 (Yang et al., 2017). Compared with current LEO instruments, GIIRS provides continuous day-and-night monitoring of atmospheric NH₃ over East Asia at approximately every two-hour interval, a breakthrough in understanding and monitoring the diurnal cycle of atmospheric NH₃ variations (Zeng et al., 2023a; Clarisse et al., 2021). A recent study by Guendouz et al. (2025) investigated the correlation between GIIRS NH₃ and surface skin temperature and showed the potential of discriminating sources between temperature-driven livestock/fertilizer volatilization and urea fertilizer application.

With over three years of FY-4B/GIIRS geostationary observations available from July 2022 to June 2025, unprecedented opportunities have emerged to monitor the spatial and temporal variations of NH₃ concentrations and their evolution throughout the day over East Asia. In this study, we highlighted the enhanced capability of GIIRS observations to identify emission sources and capture daytime variations associated with agricultural activities, surpassing those reported by polar-orbiting satellites. The data and methodology are described in Sect.2. The spatial patterns and seasonal cycles of NH₃ observed by GIIRS are compared with observations from IASI and CrIS and estimates from the MIX Asian emission inventory in Sect.3.1. The data accuracy and temporal variations of satellite-derived NH₃ are validated against ground-based Fourier Transform Infrared (FTIR) measurements at the Hefei station in Sect.3.2. The daytime variations of NH₃ from GIIRS observations and model simulations in major agricultural regions are discussed in Sect.3.3. Conclusions are summarized in Sect.4.

2 Data and Methodology

2.1 Satellite NH₃ retrievals

2.1.1 GIIRS observations

FY-4B/GIIRS was successfully launched on 3 June 2021, and operated at 133°E from 12 April 2022 to 31 January 2024. As the FY-4A satellite approached fuel depletion, FY-4B was maneuvered from 133°E to 105°E in February 2024 to take over FY-4A's observation duties, and it has been operating nominally at 105°E since 27 February 2024. FY-4B/GIIRS observations primarily covers the regions from 3°N to 55°N and 60°E to 137°E, encompassing East Asia and parts of South and Southeast Asia (Fig. 1). The instrument performs measurements over the target region every 2 hours using a "step-stare" scanning mode. Observations are conducted along 12 scanning lines from north to south, with 27 fields of regard (FORs) arranged from west to east along each line. Within a FOR is a two-dimensional infrared detector array composed of 16×8 sparsely arranged pixels. Each Pixel has a nadir-projected size of approximately 12 km × 12 km, with a spacing of 12 km in both along-track and cross-track directions between adjacent pixels. Initially, 12 measurement cycles in a day started at 00:00, 02:00, 04:00, ..., 22:00 UTC. After 6 September 2022, the start times were changed to 01:00, 03:00, 05:00, ..., 23:00 UTC, respectively.





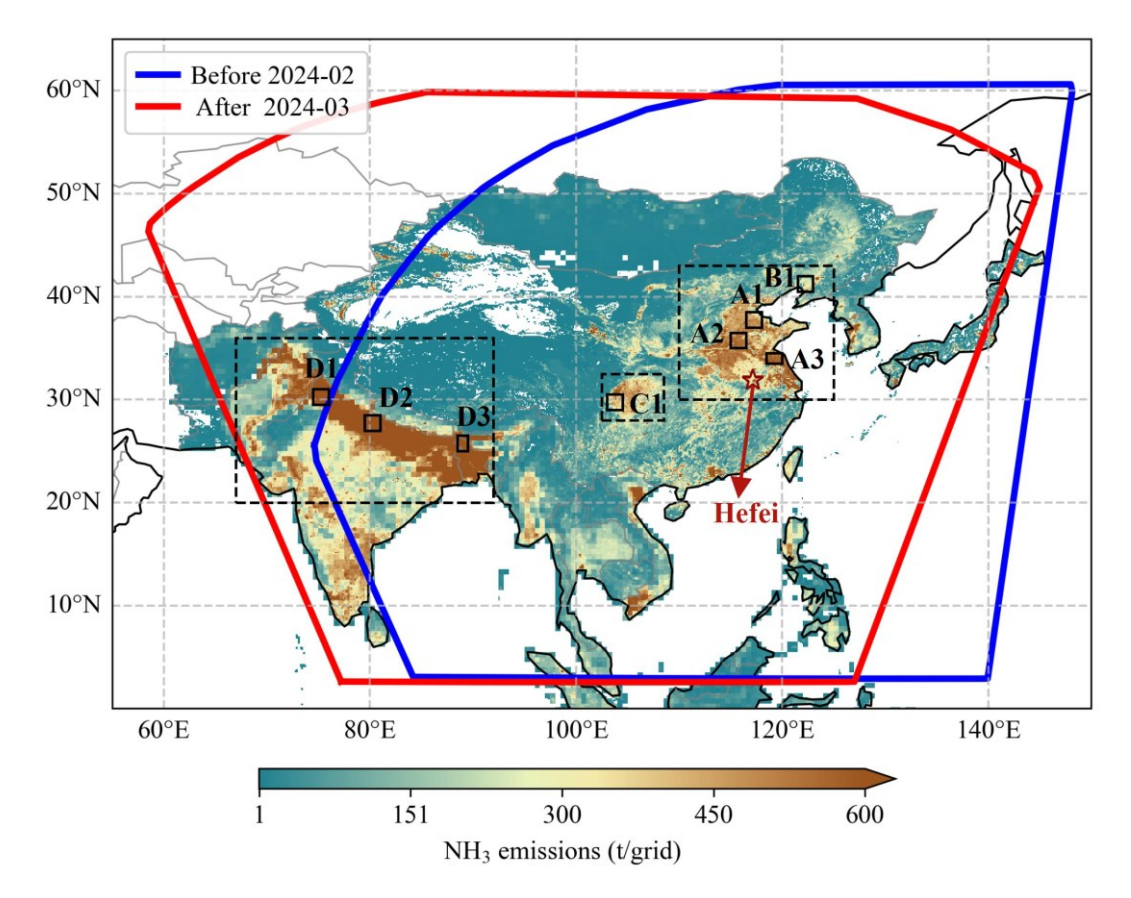


Figure 1. Spatial domain of FY-4B/GIIRS observations over East Asia. The blue and red boxes outline regions with valid NH₃ retrievals prior to and following the FY-4B orbital relocation, respectively. The background map shows total anthropogenic NH₃ emissions in 2017 from the MIX emission inventory at a 0.1° grid resolution (Li et al., 2024). The red pentagram marks the location of the Hefei station, which is further described in Sect. 3.2, and the black boxes (A1-A3, B1, C1, D1-D3) indicate major agricultural areas discussed in Sect. 3.3.

Three years of NH₃ columns from July 2022 to June 2025 are retrieved from FY-4B/GIIRS spectra using the FengYun Geostationary satellite Atmospheric Infrared Retrieval (FY-GeoAIR) algorithm, which exploits the strong NH₃ absorption features in the 955–975 cm⁻¹ spectral region. FY-GeoAIR is a full-physics retrieval algorithm that integrates a forward radiative transfer model for simulating upwelling thermal radiation and an optimal estimation-based inverse model for retrieving trace gases and auxiliary parameters from the observed spectra (Zeng et al., 2023a). In this study, the retrieval configuration and parameters are identical to those described in Zeng et al. (2023b), except that a "profile-scaling retrieval" approach was adopted instead of the "full-profile retrieval" method, which retrieves partial NH₃ columns at each atmospheric layer. In contrast, the profile-scaling retrieval applies a single, representative a priori profile (identical for all scenes) and scales this profile in the retrieval algorithm to optimize the spectra fitting. The retrieval yields the NH₃ column and the posteriori error estimate, as well as the column averaging kernel (AVK) from surface to 200 hPa (See examples in Fig. S1). This retrieval strategy is similar to the Total Carbon Column Observing Network (Wunch et al., 2011). The column AVK value at a specific atmospheric layer



154

155

156

157

158

159

160

161

162

163

164

165

166

167

168

169

170

171

172

173

174

175

176

177

178

179

180

181

182

183

184



represents the change of the retrieved total NH₃ column with respect to a perturbation of the partial NH₃ column at that atmospheric layer.

The observations that are cloud-contaminated or fail to converge within 10 iterations are excluded. To obtain high-quality GIIRS NH₃ observations, we also applied the following filtering criteria: (1) a root mean square error (RMSE) of the fitting residual less than 0.2 K; (2) a reduced χ^2 less than 5; (3) retrieval error below 300%; (4) the absolute difference of the a priori and retrieved surface skin temperature less than 10 K; (5) the bottom layer (from surface to \sim) of column AVK greater than 0.1; (6) the thermal contrast (TC) greater than 0 K; (7) the retrieved NH₃ columns are positive. The retrieval error was calculated as the square root of the diagonal elements of the retrieval error covariance matrix for NH₃, normalized by the ratio of the retrieved NH₃ column to the a priori NH₃ column. The TC is defined as the temperature difference between the surface and the lowest atmospheric layer. In this study, NH₃ retrievals from individual observations over land during daytime (7:00–19:00 LST) were utilized to investigate spatial and temporal variations over East Asia (Fig. 2). To facilitate regional analysis, individual retrievals were averaged onto a $0.5^{\circ} \times 0.5^{\circ}$ grid. The strict quality filtering results in large data gaps over the Tibetan Plateau throughout the day, and over southern regions of China and India during 17:00–19:00 LST, where retrievals are frequently discarded due to low sensitivity or cloud screening. For the analysis of daytime NH₃ variations presented in Sect. 3.3, we further filtered the daytime observations by requiring TC > 5 K to ensure sufficient sensitivity to near-surface NH₃.

2.1.2 IASI observations

The IASI instrument, jointly developed by the Centre National d'Études Spatiales (CNES) and the European Organisation for the Exploitation of Meteorological Satellites (EUMETSAT), was specifically designed for deployment aboard the Metop series satellites. Three identical instruments were successively embarked on the Metop-A, Metop-B and Metop-C platforms, launched in 2006, 2012 and 2018, respectively. IASI operates in a sun-synchronous LEO at an altitude of approximately 800 km, with a ground swath of ~2100 km and a spatial resolution of 12 km at nadir. It measures the Earth's emitted infrared radiation across a spectral range of 645-2760 cm⁻¹ with an apodized resolution of 0.5 cm⁻¹ (Clerbaux et al., 2009). The nearreal-time NH₃ dataset is retrieved using the Artificial Neural Network for IASI (ANNI) framework. This method converts the hyperspectral signature of NH₃, quantified by the so-called hyperspectral range index (HRI), into total column amounts (Whitburn et al., 2016). Two independent validation studies demonstrated that IASI-retrieved NH₃ columns show good consistency with both in situ and FTIR observations, exhibiting near-unity regression slopes and moderate biases (Guo et al., 2021; Wang et al., 2020). In this study, we utilized NH₃ data from IASI observations on the Metop-B and Metop-C platforms from January 2017 to June 2025 for comparison with GIIRS observations. The data products provide total NH₃ columns derived from the ANNI version 4 algorithm, which is about 15-20% larger than the previous version 3 due to the improved setup of HRI, but show very similar NH₃ distribution (Clarisse et al., 2023). Here, NH₃ columns marked as recommended by both pre-filter and post-retrieval quality flags in the data products were selected and then regridded onto a 0.5° spatial grid using arithmetic averaging. The quality flags allow some negative columns to be retained, as discussed by Clarisse et al. (2019) and Whitburn et al. (2016).



185

186

187

188

189

190

191

192

193

194

195

196

197

198

199

200

201

202

203

204

205

206

207

208

209

210

211

212

213

215



2.1.3 CrIS observations

The Cross-track Infrared Sounder (CrIS) is a Fourier transform spectrometer (FTS) jointly developed by the National Oceanic and Atmospheric Administration (NOAA) and the National Aeronautics and Space Administration (NASA), provides hyperspectral infrared measurements at a spectral resolution of 0.625 cm⁻¹ with a nadir spatial resolution of ~14 km. CrIS was first launched on the Suomi National Polar-orbiting Partnership (S-NPP) satellite on 28 October 2011 and subsequently deployed on NOAA-20 (JPSS-1) on 29 November 2017 and on JPSS-2 on 10 November 2022. The NH₃ retrievals from CrIS observations on S-NPP and NOAA-20 have been generated using the CrIS Fast Physical Retrieval (CFPR) algorithm developed by Environment and Climate Change Canada (ECCC), which exploits spectral features near 967 cm⁻¹. A detailed description of the CFPR algorithm can be found in Shephard et al. (2015, 2020). Independent validation studies against FTIRderived total column measurements have demonstrated that CFPR (version 1.3) shows good overall consistency, with a correlation of approximately 0.8 and a slope of 1.02. For retrievals with total column values above 1×10¹⁶ molec/cm² (ranging from moderate to high levels), the relative bias is less than 5 %. For smaller total column values ($< 1 \times 10^{16}$ molec/cm²), there are larger differences, with CrIS retrievals about 30% higher than FTIR values (Dammers et al., 2017a). However, these validations did not account for non-detects (White et al., 2023) below the detection limit of the sensor (~4×10¹⁵ molec/cm² under typical remote sensing conditions) (Shephard et al., 2025), which could reduce potential high-biases over non-source conditions. In this study, we used CrIS NH₃ data product from NOAA-20 (version 1.6.4), spanning the period from March 2019 to April 2025. The product provides geolocation information, vertically integrated ammonia total columns, retrieval uncertainties, quality flags, and additional metadata. Our analysis focuses on NH3 retrievals over land, characterized by land fraction > 0, quality flag ≥ 4 , cloud flag $\ne 1$, and DOFS ≥ 0.1 .

2.2 Ground-based FTIR measurements at Hefei

The Hefei station (31.91°N, 117.17°E) is located in the northwestern rural area of Hefei city, China. The surrounding region is part of the typical Jianghuai agricultural region, where wetlands and croplands are interspersed in a distinctive landscape pattern. Since July 2015, a high-resolution ground-based Fourier transform infrared spectrometry (FTIR) has been operated at the station to record mid-infrared (MIR) solar absorption spectra (700–4000 cm⁻¹) for the remote sensing of greenhouse gases and trace species (Wang et al., 2017). Previous studies have demonstrated that FTIR measurements at Hefei effectively capture spatiotemporal variability of NH₃ columns, with retrievals showing broadly consistent with IASI satellite data (Wang et al., 2022). In this study, FTIR-derived NH₃ column data from 2017 to 2024 were averaged to hourly means and used for the validation and cross-comparison of satellite-based NH₃ retrievals. Noted that the data primarily covers the period from 8:00 to 17:00 LST, with limited available observations between 17:00 and 18:00 LST.

214 2.3 NH₃ emission inventory

In this paper, the anthropogenic emission data of NH₃ in 2017 from the MIX v2.3 inventory was used for a comparison



222

223

224

225

226

227

228

229

230

232

233

234

235

236

243

244



with the NH₃ concentrations observed by satellites. MIXv2.3 is a mosaic emission inventory for Asia for the years 2010-2017, which is developed to support the Model Inter-Comparison Study for Asia Phase IV (MICS-Asia IV) project by a mosaic of up-to-date regional and national emission inventories (Li et al., 2024). MIXv2.3 provided monthly NH₃ emissions estimates for seven sectors, including agriculture, power, industry, residential, transportation, open biomass burning and shipping. The spatial domain covers 23 countries and regions in East, Southeast and South Asia, with a spatial resolution of 0.1°× 0.1° grid.

2.4 Hourly NH₃ data from GEOS-CF model

The Goddard Earth Observing System composition forecast (GEOS-CF) system is a high-resolution global constituent prediction model developed by NASA's GMAO. It expands on the GEOS weather and aerosol modeling system by introducing the GEOS-Chem chemistry module, providing near-real-time, three-dimensional gridded information on atmospheric composition (Keller et al., 2021). The emission inputs of anthropogenic NH₃ emissions used by GEOS-CF are mainly from the Hemispheric Transport of Air Pollution emissions inventory (HTAP v2.2), which is monthly data at a 0.1° spatial resolution. The model runs at hourly intervals with 0.25°×0.25° horizontal resolution and 72 hybrid-eta levels from the surface to 0.01 hPa. In this study, NH₃ vertical profiles were obtained from 1-day replay simulations (referred to as "hindcast") constrained by pre-computed meteorological analysis fields, and NH₃ total columns were calculated by combining the model's vertical pressure levels and surface pressures from the fifth-generation ECMWF reanalysis (ERA5) (Hersbach et al., 2023).

231 2.5 The derivation of NH₃ variations

2.5.1. Curve-fitting Method for trend analysis

To quantify the temporal changes in NH₃ columns, we applied a curve-fitting method to obtain daily time series of satellite-based NH₃ observations. This method is widely used to extract temporal variation characteristics of atmospheric composition, such as NH₃ (Wang et al., 2022; Van Damme et al., 2015). As shown in Eq. (1), it integrates a polynomial function and a sum of harmonic function, representing long-term linear trend and seasonal cycles, respectively.

237
$$f(t) = a_0 + a_1 t + \sum_{n=1}^{4} (\beta_n \sin(2n\pi t) + \gamma_n \cos(2n\pi t))$$
 (1)

where f is the daily fitting result, t is the time in decimal years, the coefficients $(a_0, a_1, \beta_n, \gamma_n)$ are determined by the least squares regression. In Sect. 3.1, the fitting analysis was performed separately for each $0.5^{\circ} \times 0.5^{\circ}$ grid cell, with more than 500 data points and observation dates spanning over 100 days. Extreme values and minima of the fitted curves were then calculated to identify temporal inflection points and determine the months with peak NH₃ concentrations.

242 2.5.2. Gridded NH₃ enhancements

Based on the spatial distribution of NH₃ emissions and concentrations, the study domain was divided into 14 subregions (Fig. 6). Monthly variations of NH₃ columns for each subregion were obtained by aggregating the daily fitted values calculated





in Sect.2.5.1, which represent the regional background levels. NH₃ anomalies from individual measurements were then calculated by subtracting NH₃ backgrounds, as defined in Eq. (2).

$$A_i = X_i - BK_{r,m} \tag{2}$$

Where A_i is the NH₃ anomaly for the individual *i*-th retrieval, X_i is the observed NH₃ column, and BK_{r,m} represents the NH₃ background for the region r and month m corresponding to the spatial location and observation time of retrieval i. For each grid cell, positive anomalies with occurrences of elevated concentrations (> 1.0×10^{16} molec/cm²) exceeding 30 days were classified as NH₃ enhancements. The frequency of such occurrences, expressed in number of days, serves as a useful indicator of enhanced emissions, such as recurring agricultural activities (Shephard et al., 2020; Warner et al., 2016).

3 Result and discussion

3.1 Spatial and temporal NH₃ distribution over East Asia

Figure 2 illustrates the three-year averaged seasonal NH₃ column concentrations retrieved from FY-4B/GIIRS observations over East Asia from July 2022 to June 2025, presented on a 0.5° by 0.5° grid at two-hour intervals. Elevated NH₃ columns, significantly above background levels, are observed over the Indo-Gangetic Plain, the North China Plain, the Sichuan Basin, and the Northeast China Plain (dashed boxes in Fig. 1). The daytime NH₃ columns reach values exceeding 4×10¹⁶ molec/cm², primarily driven by intensive agricultural activities and supplemented by non-negligible contributions from urban and industrial emissions. Localized weaker enhancements of NH₃ column concentrations are evident over agricultural core areas in China (including the Ningxia Irrigation Plain, the Wei River Plain, the Jianghan Plain, and oasis agriculture in the arid regions of Xinjiang), as well as the central Deccan Plateau in India, the Mekong Delta in Vietnam, the Chao Phraya River Plain in Thailand, and the Fergana Valley in Uzbekistan (dashed boxes in Fig. S3). Most of these regions exhibit higher NH₃ columns in summer and considerable daytime variability, with large differences between morning and afternoon observations. A detailed analysis of diurnal patterns over major source regions is provided in Sect. 3.3.



269



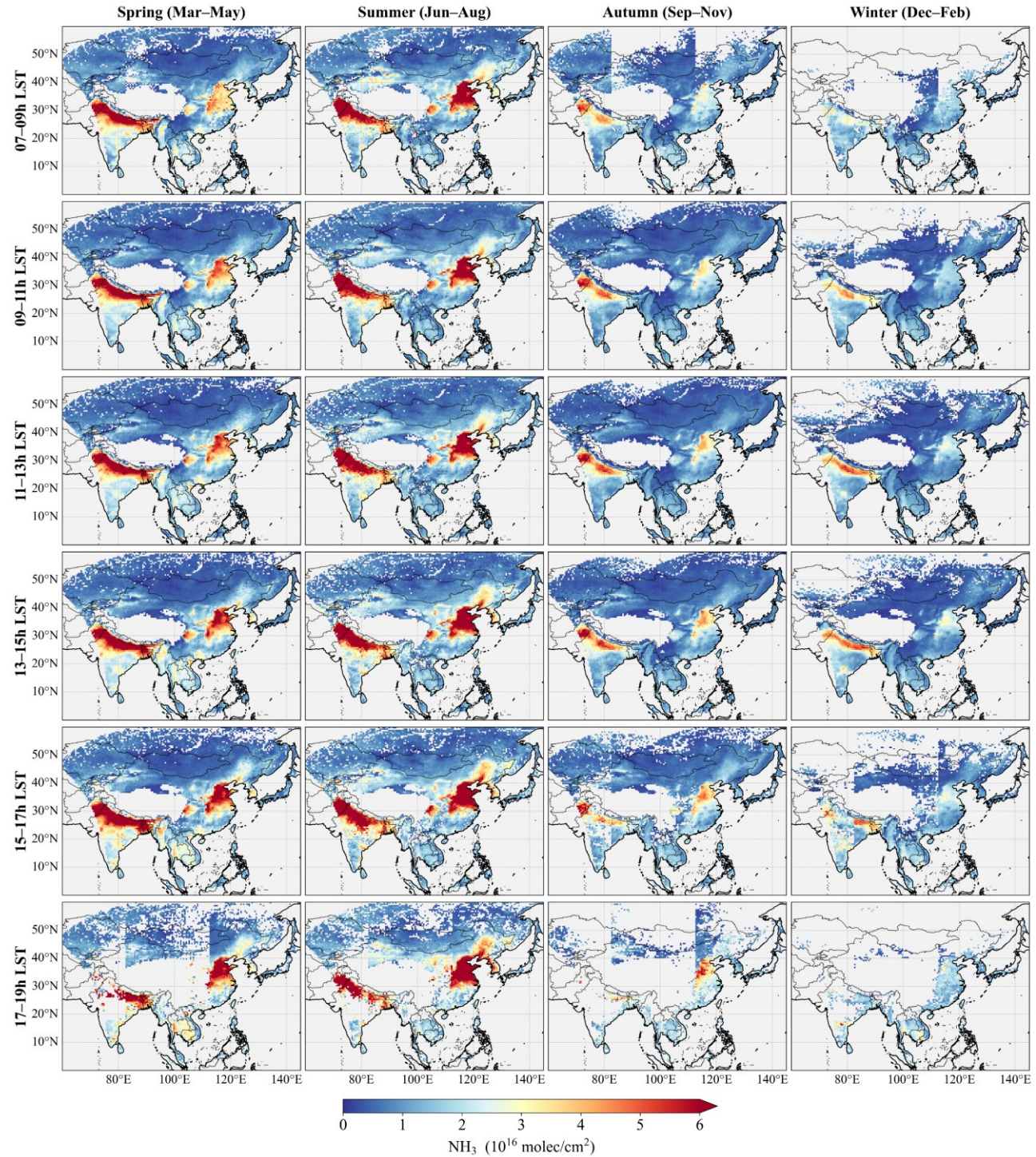


Figure 2. Seasonal maps of NH₃ columns from FY-4B/GIIRS observations from July 2022 to June 2025 averaged for every 2 hours according to local solar time (LST) on a 0.5° by 0.5° grid and for different seasons (spring: March-April-May; summer: June-July-August; autumn: September-October-November; winter: December-January-February).





Comparisons with the spatial distribution of NH₃ columns observed by polar-orbiting infrared sounders of IASI and CrIS show reasonable agreement, especially in regions with high NH₃ columns above 3×10¹⁶ molec/cm² (Fig. 3 and Fig. 4). The seasonal increases in atmospheric NH₃ are most pronounced in spring and summer. Despite generally similar seasonal and spatial patterns, inter-satellite NH₃ observations exhibit noticeable differences. Relative to the IASI observations, GIIRS typically shows very small systematic differences with fitted slopes close to unity. In contrast, GIIRS observations tend to show higher NH₃ columns than CrIS in most high-concentration regions, with mean summer differences of approximately 25–50% relative to the corresponding GIIRS values. The data point scattering in the comparison plots primarily results from spectral noise. Overall, there is good agreement between GIIRS-derived NH₃ columns and those from IASI and CrIS across different seasons.

To account for the effects of differing vertical sensitivities, as reflected by the AVKs, and a priori profiles among these satellites (see Fig. S1 for examples), we conducted experiments using model profile data and satellite AVKs over the North China Plain and the Northeast China Plain (30°–43°N, 110°–125°E) in June 2024 (Text S1). Model simulations of NH₃ profiles were convolved with different satellite AVKs to generate AVK-smoothed NH₃ columns, representing the NH₃ columns that a certain satellite would retrieve if the model simulations were the "truth". We then compared AVK-smoothed NH₃ column datasets generated different satellite AVKs to evaluate the effects of different satellite vertical sensitivities. The comparison results (Fig.S5) show high correlations (R >0.9) and slopes close to 1. This indicates consistency in the detection of NH₃ across different sensors, and that the effects of different AVKs and a priori profiles are small in terms of total column retrieval when comparing different satellite retrievals.





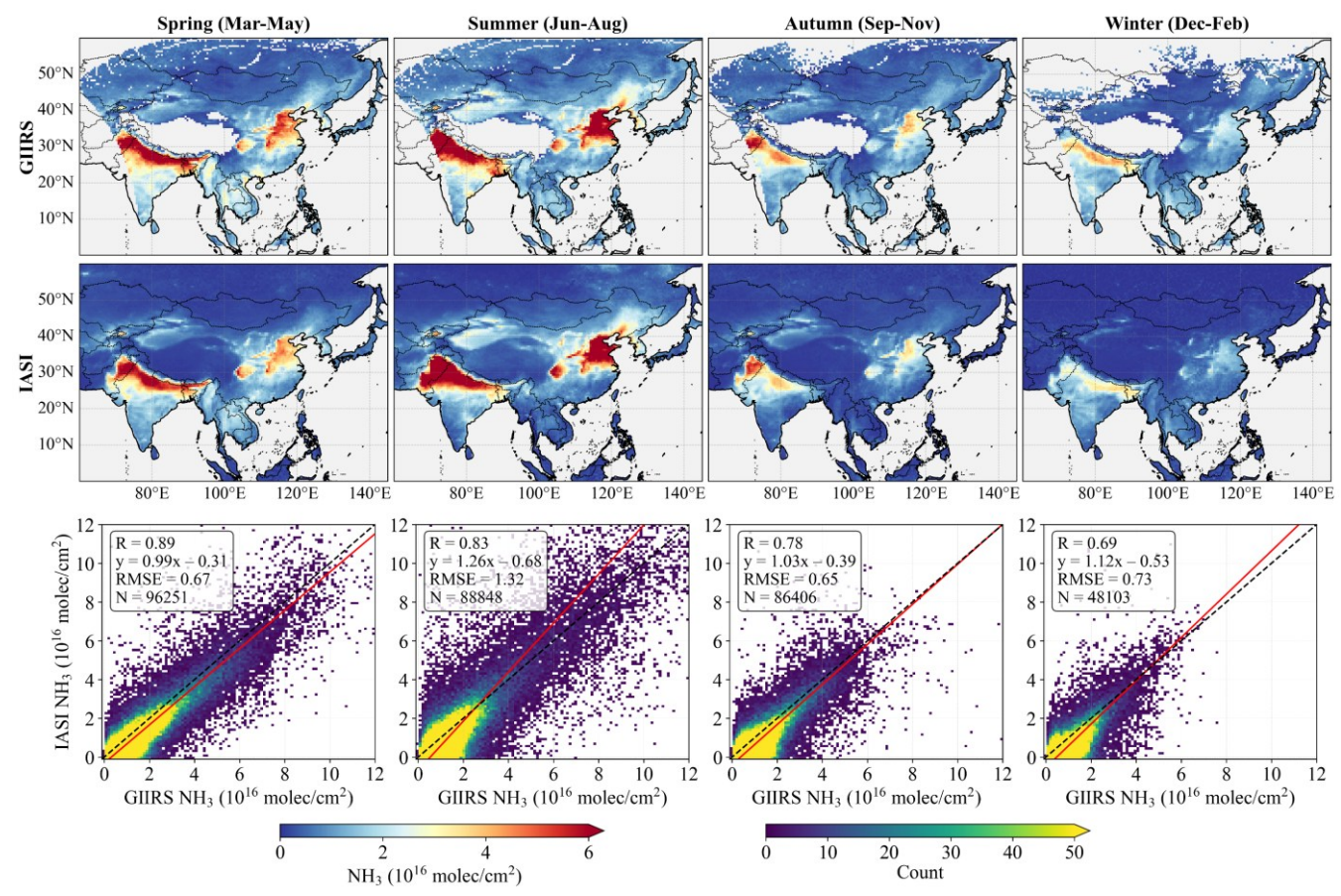


Figure 3. Comparison of NH₃ columns observed by GHRS and IASI during morning overpasses (\sim 09:30 LST) from July 2022 to June 2025. Seasonal maps are presented on a $0.5^{\circ} \times 0.5^{\circ}$ grid. Scatter plots compare monthly mean NH₃ columns within the same grid cells and hourly intervals.





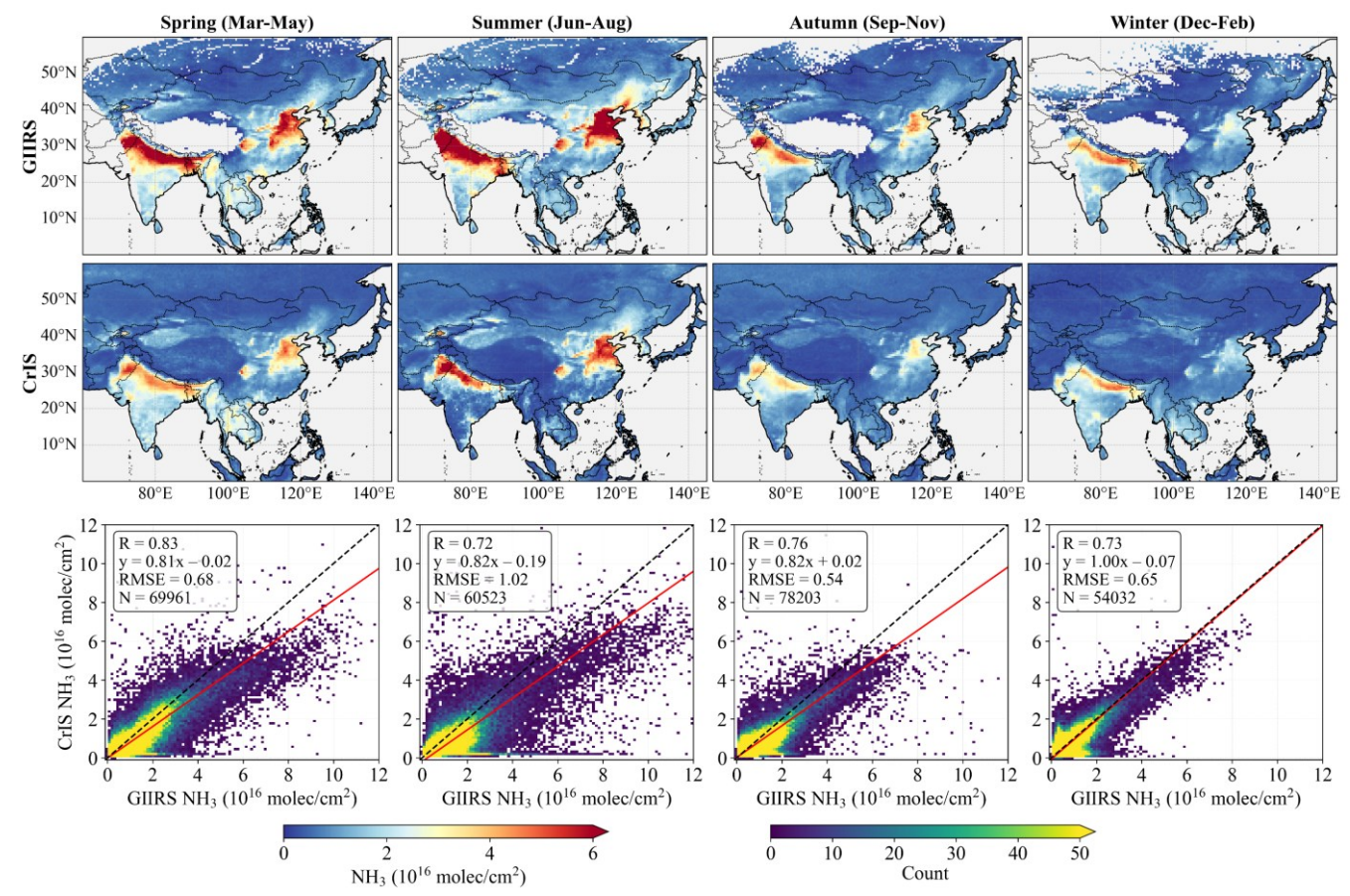


Figure 4. Comparison of NH₃ columns observed by GIIRS and CrIS during afternoon overpasses (~13:30 LST) from July 2022 to April 2025, using the same methodology as in Fig. 3.

Figure 5 illustrates the months corresponding to the maximum NH₃ concentrations derived from GIIRS and IASI at a 0.5° grid, while the result from CrIS, which is highly scattered at this scale, is shown at 1° grid in Fig. S5. The spatial pattern shows a clear north-south gradient in the timing of NH₃ peaks. In the northern regions of East Asia, NH₃ columns generally peak in June and July, which could be attributed to enhanced volatilization from agricultural soils, livestock operations, and other sources (e.g., composting facilities and wastewater treatment plants) under high-temperature conditions (Li et al., 2024). Irrigated croplands in the North and Northeast China Plains also exhibit a secondary spring maximum (Fig. S6) associated with extensive fertilizer use and animal feeding operations. In contrast, the regions of southern China, India, and Southeast Asia, characterized by a tropical monsoon climate, exhibit earlier NH₃ peaks, generally occurring from March to May. The peak period coincides with their first cropping season, which involves intensive nitrogen fertilizer application. The warm and humid conditions in these regions further promote NH₃ volatilization from soils and livestock waste. Following the onset of the rainy season in June-July, atmospheric NH₃ concentrations decline sharply (such as R7, R8, R13, R14 in Fig. 6), primarily due to enhanced wet scavenging processes. This seasonal pattern aligns with findings from multiple studies reporting a distinct





"late dry season-early wet season" NH₃ maximum in tropical regions (e.g., Chen et al., 2020; Liu et al., 2019). In addition, bimodal local maxima, with peaks of comparable magnitude, are also observed in regions such as central India (from May to September), Guangdong in southern China (typically in April and August), and the transboundary region between the Mekong Delta in Vietnam and Yunnan in China (March-April and June-July). The consistent spatial distribution of NH₃ observed by GIIRS and IASI over Southeast Asia also reflects the influence of biomass burning associated with fires on its seasonal variations. In general, the spatial and temporal distributions largely agree with the previous studies of Van Damme et al. (2015) and Shephard et al. (2020). Minor discrepancies between GIIRS and IASI result from differences in observational accuracy and retrieval algorithms, as discussed above. The results indicate that satellite-observed NH₃ seasonal cycles are driven by the interplay of agricultural activities and climatic conditions, leading to deviations from seasonal patterns of anthropogenic emissions (Fig. 6).

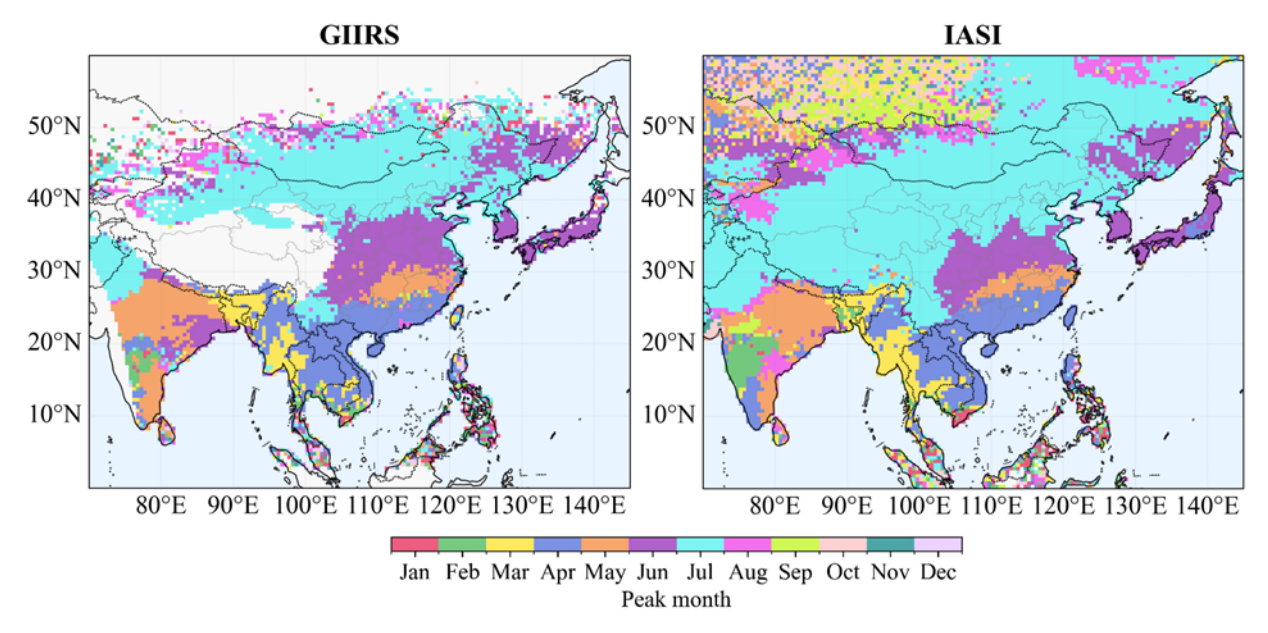


Figure 5. The months with NH₃ column peaks observed by FY-4B/GIIRS from July 2022 to June 2025 and IASI from January 2022 to June 2025 at a $0.5^{\circ} \times 0.5^{\circ}$ grid. GIIRS results for the full daytime period (07:00–19:00 LST) are presented here for clarity, as morning and afternoon observations show consistent seasonal patterns (not shown).





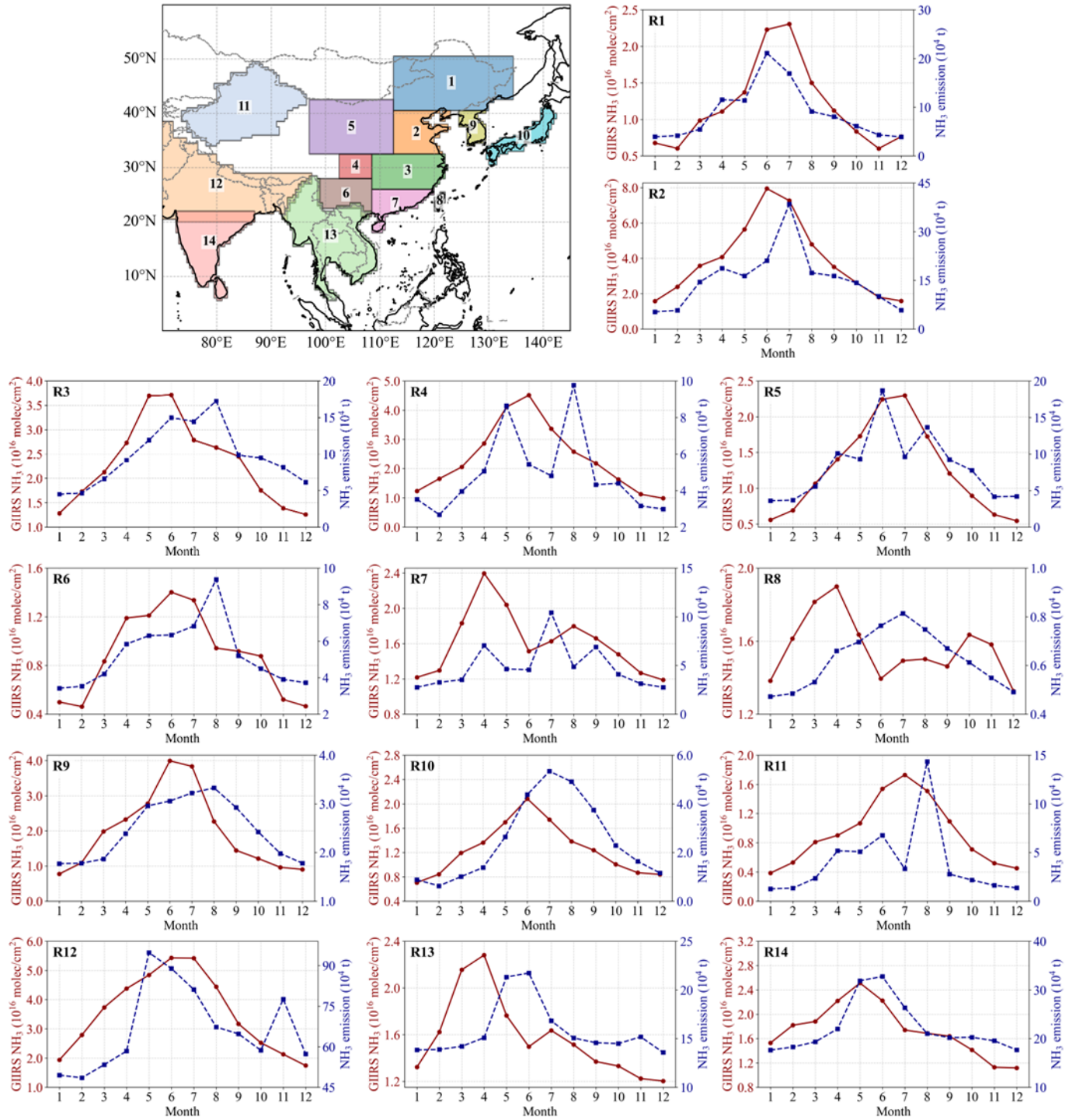


Figure 6. Monthly variations of GIIRS-derived NH₃ columns from July 2022 to June 2025 and NH₃ total emissions from the MIX inventory in 2017. Coloured boxes specify domains of 14 subregions (Sect. 2.5.2).





After removing monthly backgrounds derived from predefined regions (Fig. S7), satellite-observed NH₃ enhancements (Fig. 7) reveal a spatial pattern of anthropogenic emissions that is highly consistent with the MIX emission inventory (Fig.1). Due to data discrepancies, the enhancement values detected by CrIS are 0.50 ± 0.64 and $0.74 \pm 0.90 \times 10^{16}$ molec/cm² lower than those detected by GIIRS and IASI, respectively. Apart from the major agricultural emission regions mentioned above, some regions (e.g. Hyderabad and Vijayawada in India) also show elevated NH₃ levels compared to the background during autumn and winter, likely influenced by dense urban and industrial activities. Differences in local overpass times and sensor sensitivities among the polar-orbiting and geostationary satellites can lead to inconsistencies in the observed NH₃ concentrations across various source regions, particularly in the Sichuan Basin, the Ningxia Irrigation Plain, and the urban and biomass-burning regions of Southeast Asia. Compared with IASI and CrIS observations at different local times, GIIRS provides consistent and reliable measurements throughout the full daytime, enabling accurate characterization of spatial and temporal variations in NH₃ concentrations across distinct emission source regions.

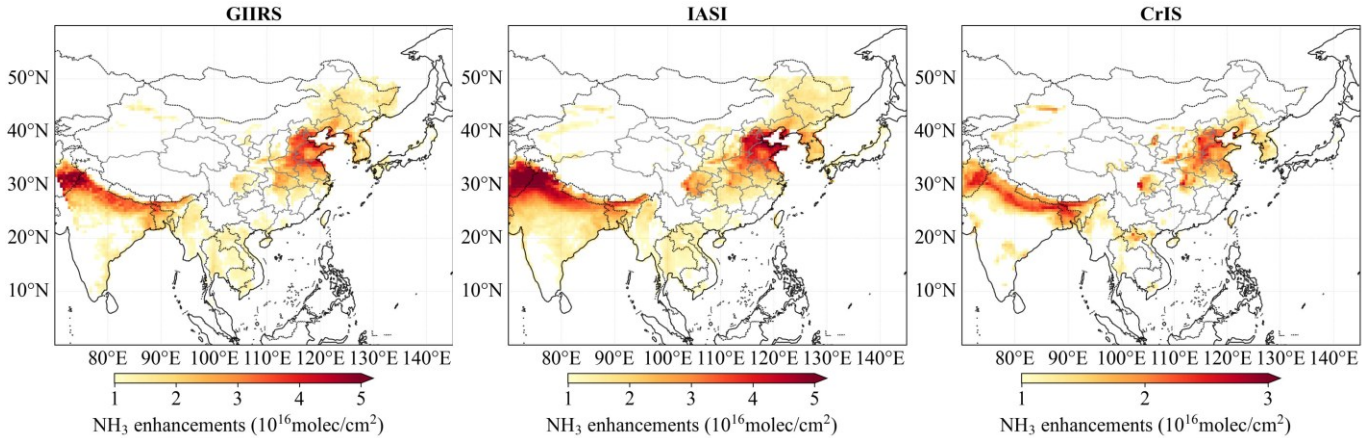


Figure 7. Spatial distribution of NH₃ enhancements derived from satellite observations (GIIRS, IASI, and CrIS). Note that the color bar for CrIS differs from those for GIIRS and IASI, and abnormal NH₃ enhancements over the Tibetan Plateau and Tibet have been excluded.

3.2 Inter-comparison of NH₃ variations at the Hefei station

To evaluate the data accuracy of GIIRS-derived NH₃ columns and assess the consistency of temporal variations with polar-orbiting satellite measurements, we compared the satellite-based observations with ground-based FTIR measurements at the Hefei station. Satellite data within a 0.25° latitude/longitude radius around the Hefei station (Fig. S8) were selected and averaged on an hourly scale. A linear regression through the origin was applied to evaluate the proportional agreement between the datasets.

Figure 8 shows scatter plots comparing NH₃ columns retrieved from satellite observations and FTIR measurements during their overlapping periods. Overall, the satellite-derived NH₃ columns show good agreement with the FTIR data, with Pearson correlation coefficients (R) exceeding 0.70, although satellite values are generally slightly higher. Among the satellites, GIIRS agrees best with FTIR in terms of highest correlation and the low root mean square error (RMSE). However, GIIRS exhibits a



relative systematic bias toward overestimating NH_3 columns, as indicated by its regression slope (1.12) being notably larger than those of IASI and CrIS. When measurement uncertainties were taken into account, regression analysis using the orthogonal distance regression (ODR) method yielded a further improvement in correlation (R = 0.80), while the regression slope increased to 1.24 (Fig. S9), demonstrating that GIIRS tends to produce consistently higher NH_3 columns than IASI and CrIS.

Although the overestimation of GIIRS becomes more pronounced in afternoon observations (Fig. S10), the corresponding data conversely show improved consistency, which is characterized by higher R and lower RMSE values. This is related to the fact that the inversion accuracy of GIIRS observations is affected by TC and boundary layer conditions. High NH₃ columns and significant TC represent favorable conditions for retrieving NH₃ from satellite observations (Zeng et al. 2023a; Clarisse et al., 2010). As illustrated in Fig. S11, large positive TC between 11:00 and 15:00 LST enhances measurement sensitivity, leading to lower retrieval errors. GIIRS NH₃ column retrievals are most reliable during daytime hours (07:00–19:00 LST), particularly in summer when TC exceeds 5 K.

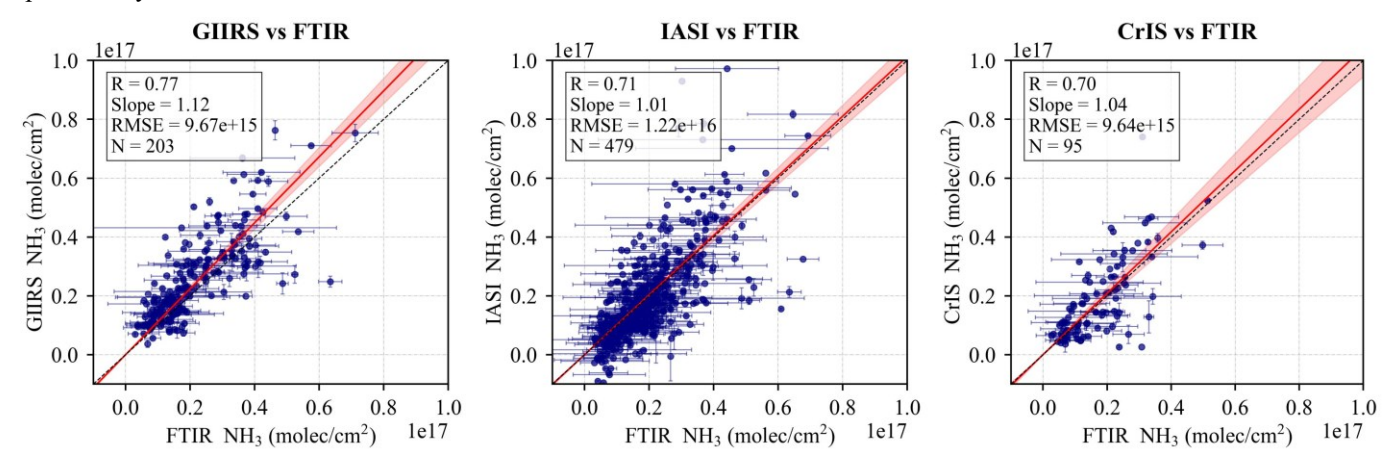


Figure 8. Cross-validation of hourly NH₃ columns from GIIRS, IASI, and CrIS with FTIR measurements at the Hefei station. The overlapping periods span January 2017 (IASI), March 2019 (CrIS), and July 2022 (GIIRS) to December 2024.

The Hefei station and its surrounding regions predominantly adopt a rice—wheat rotation, with rice and winter wheat typically sown in spring (around May) and autumn (around October), respectively. According to the MIX emission inventory, agricultural ammonia emissions in this region exhibit two primary peaks in June and August, which are associated with local agricultural practices including livestock waste management, nitrogen fertilizer application and irrigation activities during the rice growing season (Hou et al., 2020). Smaller peaks occur in October-November and April, corresponding to the rice harvest/wheat sowing period and the wheat regreening fertilization stage, respectively. Driven jointly by agricultural emission intensity and meteorological conditions such as high temperatures, atmospheric NH₃ concentrations observed by satellites and ground-based FTIR show consistent seasonal cycles, peaking in summer (June—August) and reaching a minimum in winter (November—January). Figure 9 shows the monthly NH₃ time series observed by satellites and FTIR at different local overpass times. GIIRS and IASI show closely matched NH₃ peaks in June. The systematic overestimation of peak values by GIIRS





relative to CrIS and FTIR is consistent with an inherent data bias as shown in Fig. 8.

Notably, GIIRS-derived NH₃ columns in June 2024 were significantly higher than those in the same month of 2023 and 2025, with increases of 1.46- and 1.67-times during morning overpass time (~9:30 LST), and 1.35- and 2.15-times during afternoon overpass time (~13:30 LST), respectively. Such pronounced variability is likely linked to extreme weather events reported in the region, such as persistent heatwaves and abrupt drought–flood transitions (Zhou et al., 2025; Ding et al., 2024). Morning observations from IASI align with GIIRS data, showing that NH₃ concentrations in June 2024 reached 1.43 to 2.62 times the levels recorded in the years 2017–2025 (specifically, 1.59 times that of 2023 and 1.53 times that of 2025). Similar interannual changes were also captured by CrIS and FTIR in June 2024, showing that NH₃ levels increased by factors of 1.17–1.53 for CrIS and 1.40–2.28 for FTIR compared to earlier years, despite data gap in June 2023 for FTIR. Similar interannual changes were observed by CrIS and FTIR in June 2024, with NH₃ levels increasing by factors of 1.17–1.53 and 1.40–2.28 compared with previous years, respectively, despite a data gap in June 2023 for FTIR.

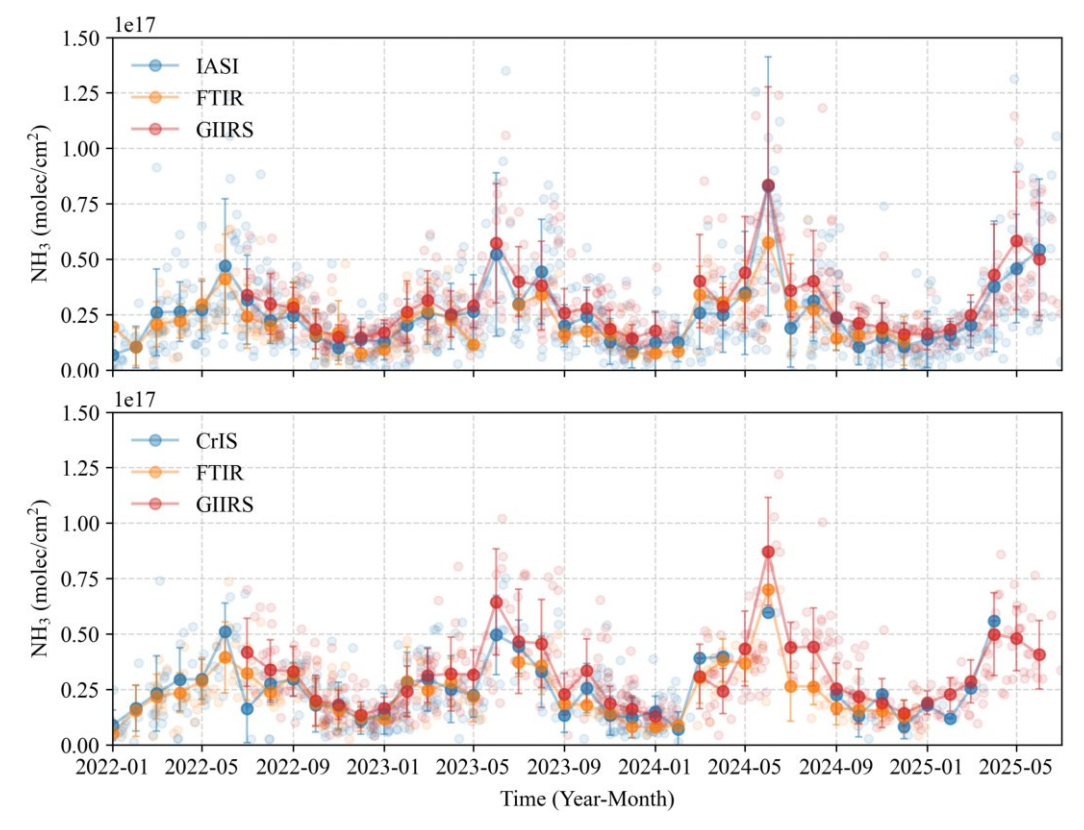


Figure 9. Timeseries of monthly NH₃ columns at the Hefei station from satellite-based and ground-based observations at different local overpass times of polar-orbiting satellites for morning (~09:30 LST) and afternoon (~13:30 LST). The light-colored, semi-transparent points represent daily mean values at different local times.

Comparing GIIRS-based NH₃ columns at different local times, afternoon concentrations are generally higher than those in the morning, with the largest differences observed in summer (July-August) and the smallest in autumn and winter. To more





accurately characterize daytime NH₃ variations, we further applied strict data filtering criteria by retaining only retrievals with TC> 5 K, to ensure the data have high sensitivity to the surface layer NH₃. Over the three-year period, 37 high-quality observation days were identified, each providing six consecutive two-hour interval observations from 07:00 to 19:00 LST (Fig. S12). The maximum diurnal amplitude occurs in summer, reaching over 1.5×10¹⁶ molec/cm². Except for autumn, all three other seasons exhibit relatively high NH₃ concentrations around 7:00 and 17:00 LST, a pattern that aligns well with the diurnal variations reported by Wang et al. (2022) based on FTIR measurements (Fig. 10). However, NH₃ retrievals from FTIR lack sufficient valid observations within a single day, making it difficult to consistently capture the intra-day variability in NH₃ across different dates.

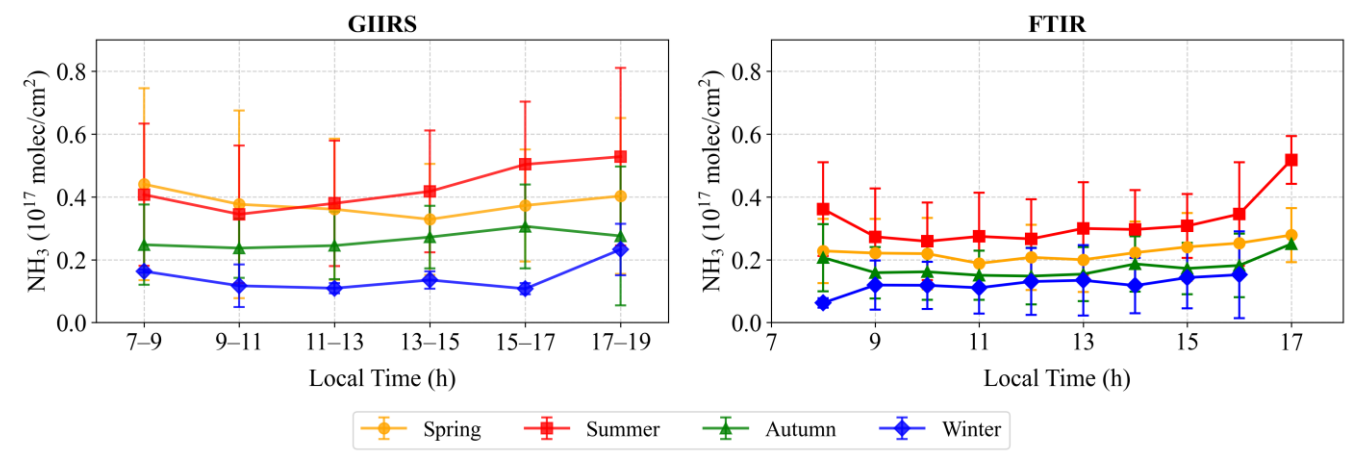


Figure 10. Daytime NH₃ variations observed by GIIRS and FTIR in different seasons. The seasonal mean NH₃ from GIIRS are calculated based on 37 high-quality days in Fig. S12.

Moreover, the FTIR station is situated in a transitional zone between the urban and suburban areas. A spatial domain with a radius of 0.25° used in this study encompasses GIIRS sampling points from both urban and agricultural regions (Fig. S8). To assess spatial variability of NH₃, GIIRS retrievals with TC > 5K within this spatial domain were classified into urban and non-urban categories, and their daytime variations were statistically analyzed across seasons over three years. As shown in Fig. S13, NH₃ concentrations in non-urban areas are consistently and significantly higher than those in urban areas during spring and summer, indicating the strong contribution of agricultural activities to ambient NH₃ levels. Particularly in spring, statistically significant differences are most pronounced during 7:00–9:00 and 17:00–19:00 LST, corresponding to time windows of fertilizer application and livestock activity. During winter, higher NH₃ levels in the morning and late afternoon are mainly observed in urban areas, likely reflecting the impact of traffic emissions. These findings highlight the importance of high-frequency satellite observations for the dynamic monitoring of NH₃ variations, and the contribution of agricultural activity in shaping the diurnal NH₃ variability.

3.3 Daytime NH₃ variations in major agricultural regions

We focused on eight major agricultural source areas with a high proportion of irrigated cropland, located in the North





China Plain and the Northeast China Plain, the Sichuan Basin, and the Indo-Gangetic Plain (black boxes in Fig. 1), to further investigate daytime variations in NH₃ columns. To ensure sufficient measurement sensitivity to near-surface NH₃, only GIIRS observations with TC greater than 5 K were retained, thereby excluding cases with low information content. Compared to the dataset used in Sect. 3.1, the fractions of valid observations remaining in the three study regions were about 83 %, 88 %, and 73 %, respectively. During autumn and winter, available observations are sparse in the early morning and late afternoon. Here, GIIRS-observed daytime variations of NH₃ columns across different seasons (Fig. 11) and the corresponding spatial distributions for each study region (Figs. 12–14) are presented, with comparisons to anthropogenic NH₃ emissions (Fig. S14) and GEOS-CF model simulations (Figs. S15–18). Despite significant differences of NH₃ columns between the model-simulated data and satellite-based observations, we focused on analyzing the daytime variations and their spatial distributions in representative months of May-June (NH₃ peak months) in 2025.

The North China Plain is characterized by extensive irrigated croplands under winter wheat—maize rotation and widespread small-scale livestock farming concentrated in east-central provinces, including Henan, Shandong, and Hebei. Due to intensive agricultural and livestock activities, dense industrial emissions and heavy urban traffic, the region ranks among the most polluted regions in China. The spatial distribution of local NH₃ high values across different seasons shows considerable variations, especially during the late afternoon in the spring and summer, which may indicate a change in emission hotspots (Fig.12). Across the three selected areas (A1-A3), GIIRS observations reveal a consistent temporal pattern of NH₃ columns, with values increasing from early morning to late afternoon in summer but generally declining after 15:00 in other seasons. In summer, the mean variations in GIIRS NH₃ column amplitudes for the afternoon and morning are 22%, 27%, and 29%, respectively, while in May and June 2025, these variations increased to 56%, 38%, and 32 %, respectively.

The Northeast China Plain is a key grain production region, particularly for maize, soybeans, and rice. Agriculture is highly mechanized, and livestock farming is carried out on a large scale. Due to concentrated emissions and fixed locations, the spatial pattern of NH₃ enhancements shows little variation at different local times (Fig. 12). The B1 area is located in the estuarine delta, with large cities such as Shenyang and Anshan to the east. Due to low population density and limited industrial activity, NH₃ emissions in this area are primarily associated with fertilizer application and animal husbandry, resulting in relatively low levels than other areas. GIIRS observations show that NH₃ columns are at markedly reduced levels, approximately 52% of those in the North China Plain, but follow a similar diurnal cycle, with the variation amplitude in summer being comparable (25% for 3 years, 43% for May-June 2015). The difference is that in winter, the diurnal variation also shows higher NH₃ columns in the morning (7:00–9:00 LST), which may be related to traffic emissions and the effects of meteorological conditions (such as temperature and humidity changes) in the early morning. Ground-based studies have reported that the peak atmospheric NH₃ concentration typically occurs in the morning, as observed in the urban area of Beijing (Gu et al., 2022) and in the rural areas of Xianghe (He et al., 2020), Xinxiang (Teng et al., 2017), Shanghai (Wang S. et al., 2015), and Hefei (Wang et al., 2022).





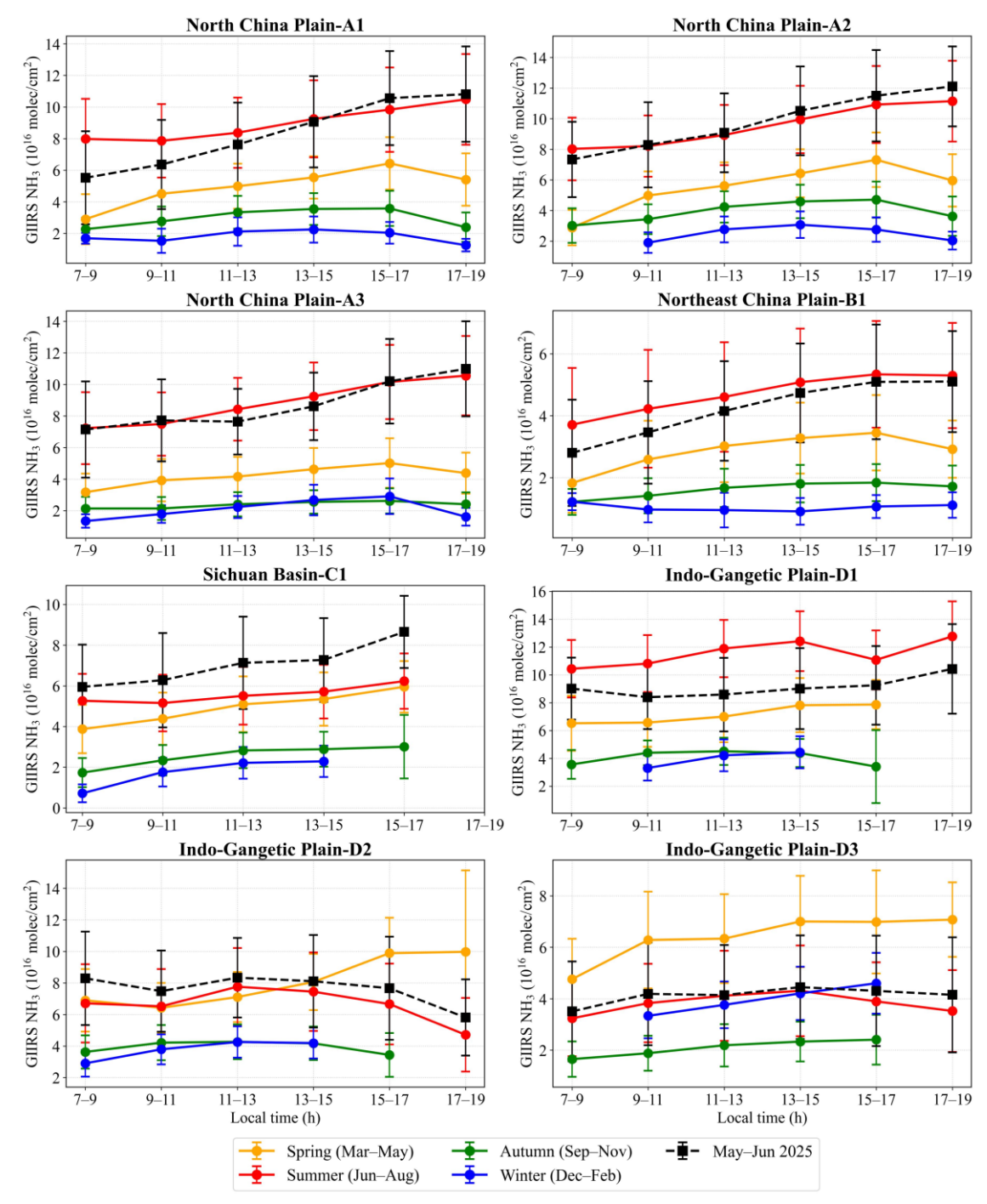


Figure 11. Daytime NH₃ variations for major agricultural emission areas observed by GIIRS in different seasons.



453

454

455



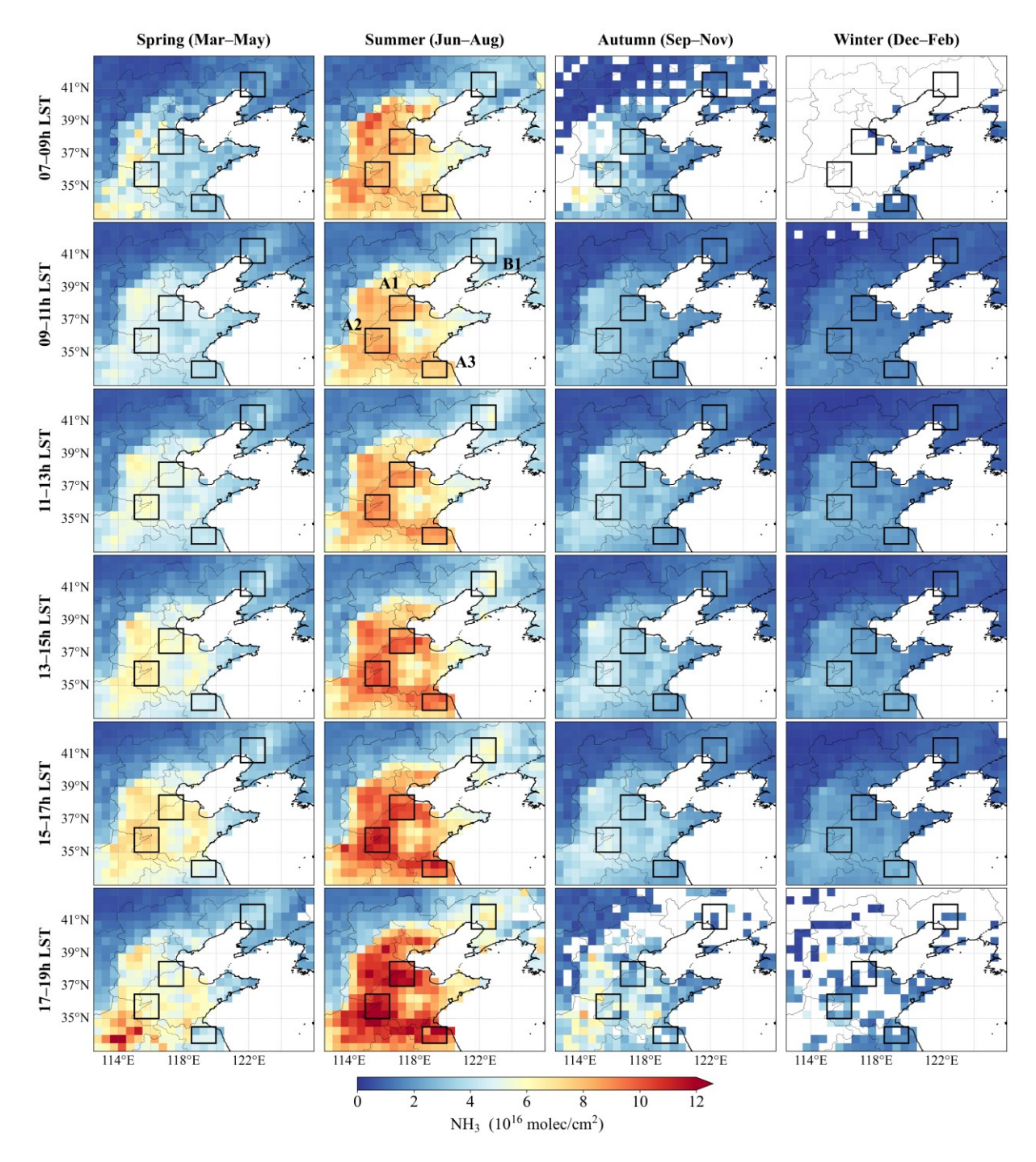


Figure 12. Daytime NH₃ variations observed by GIIRS from July 2022 to June 2025 in the North China Plain and the Northeast China Plain.

The Sichuan Basin, located in southwestern China, is an important agricultural region, producing rice, rapeseed, vegetables, and citrus fruits, with intensive irrigation and high crop density. Satellite observations show that NH₃ is





significantly enhanced in the western regions, particularly along the Mianyang-Deyang-Chengdu-Meishan-Leshan corridor (Fig. 7 and Fig.13), reflecting both intensive agricultural activity and urban-industrial emissions. The basin's unique topography and meteorological conditions such as frequent temperature inversions result in very few valid NH₃ observations after 17:00 LST. Across different seasons, NH₃ columns generally exhibit an increasing trend from morning to afternoon. In spring and summer, seasonal mean NH₃ concentrations show relatively small differences because agricultural sources dominate and vertical mixing is enhanced by changes in boundary layer height, with daytime NH₃ variations of 27% and 23%, respectively. The largest daytime variation occurs in winter, when afternoon values are 1.46 times higher than those in the morning.

The Indo-Gangetic Plain, South Asia's most extensive alluvial plain, spans Pakistan, northern India, and Bangladesh. The region is densely populated and intensively farmed, producing rice, wheat, sugarcane, and vegetables, often under irrigated and mechanized conditions. Fertilizer application, livestock excretion, industrial activities, and high population density lead to significant NH₃ and reactive nitrogen emissions, reaching their maximum over the Punjab, Pakistan. We selected three areas that are located in Punjab, Uttar Pradesh, and Bangladesh, respectively (Fig.14). Differences in NH₃ emission sources and climatic conditions across these regions lead to pronounced seasonal variations in NH₃ concentrations (Fig. S3). The daytime variation amplitudes of NH₃ columns are highest in spring, which are 17%, 32%, and 21% for D1, D2, and D3, respectively. However, under the coupled conditions of abundant precipitation and strong solar radiation in summer, NH₃ columns in the D2 and D3 areas reach their peak around 13:00 LST.





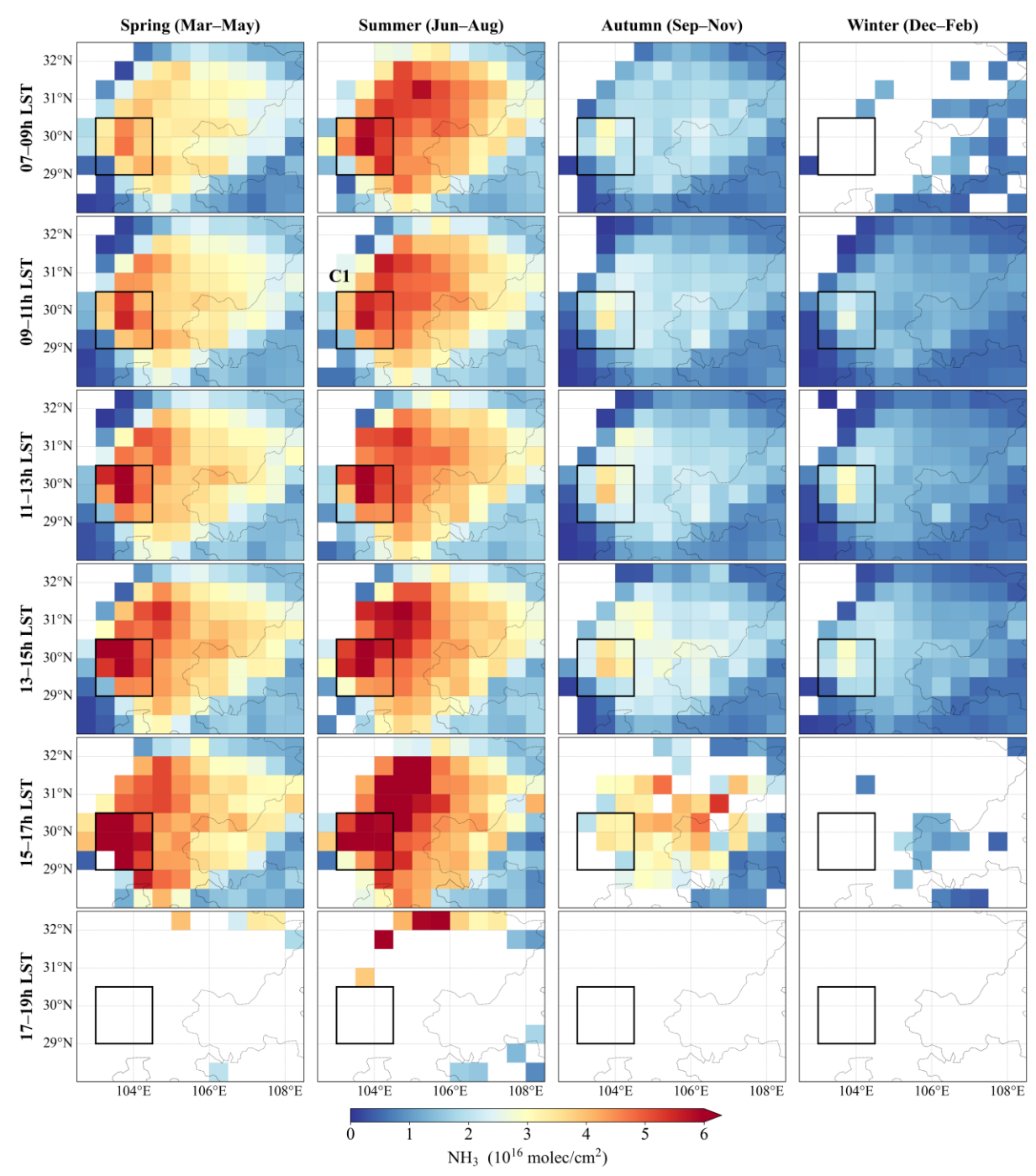


Figure 13. Daytime NH₃ variations observed by GIIRS from July 2022 to June 2025 in the Sichuan Basin.



478

479

480



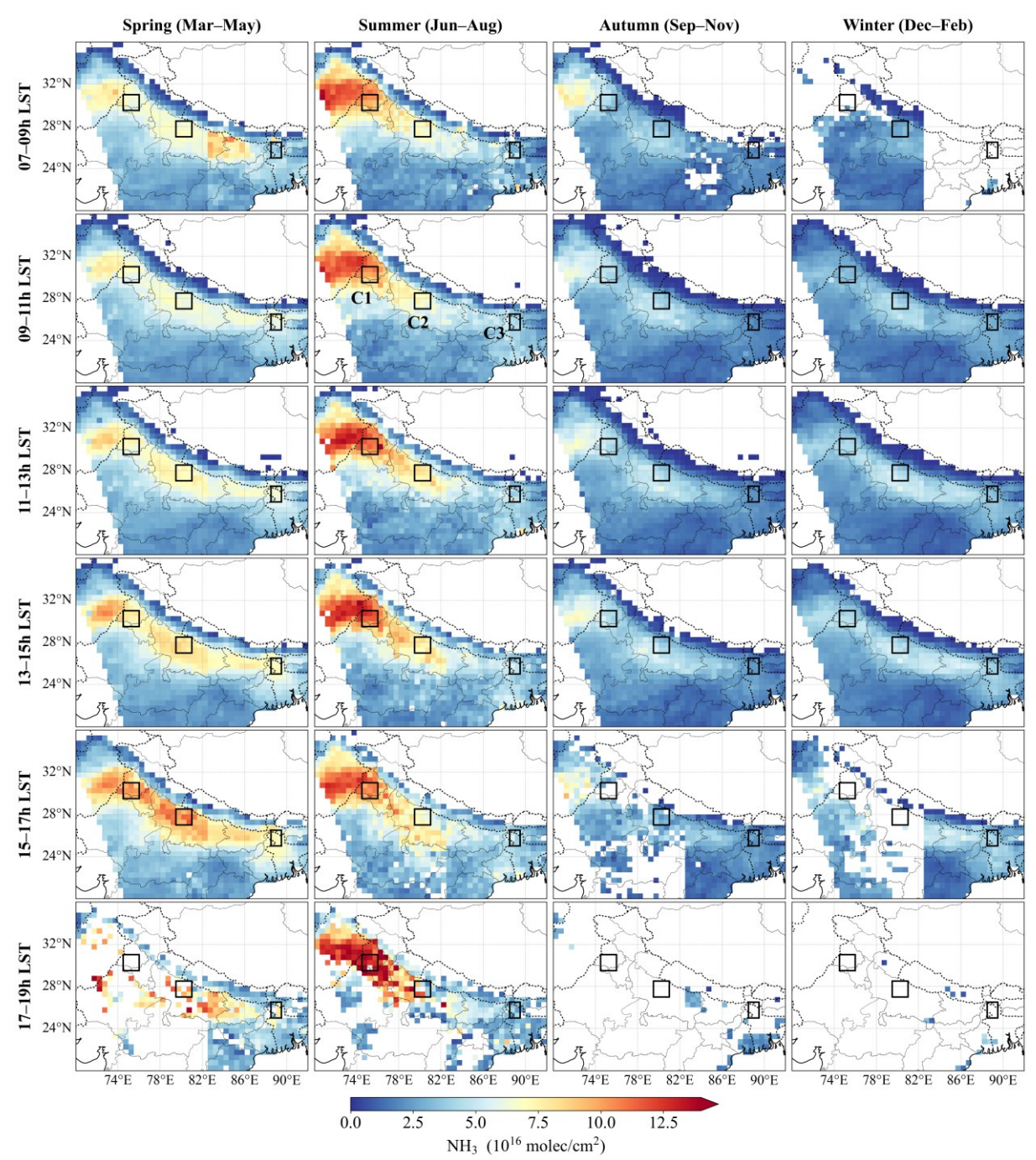


Figure 14. Daytime NH₃ variations observed by GIIRS from July 2022 to June 2025 in the Indo-Gangetic Gangetic Plain.

The diurnal variation of atmospheric NH₃ column concentrations is primarily influenced by surface emissions, boundary layer dynamics, and gas-particle partitioning associated with meteorological conditions (Behera et al., 2013; Lan et al., 2024). In these main agricultural source areas, NH₃ concentrations generally rise from morning to afternoon, which is driven by





diurnal variations in temperature and humidity that shift the gas-particle equilibrium toward the gaseous phase. The daytime NH₃ variations simulated by the GEOS-CF model for May-June 2025 range from 7% to 36%, which is slightly lower than the variations observed by GIIRS (10% to 56%). However, the GEOS-CF model was unable to accurately reproduce the spatial pattern of NH₃ enhancements in the Sichuan Basin (Fig. S17), which can be largely attributed to the influence of complex topography and local climatic conditions. After considering about the vertical sensitivities of satellite retrievals, the AVK-smoothed model data resulted in an overall reduction of 12 ± 38% in the model NH₃ columns over the Sichuan Basin. However, considerable discrepancies in the spatial distribution remain relative to the satellite observations. Figure 15 presents a cross-comparison between the satellite-derived NH₃ columns and the AVK-smoothed model data in May-June 2025. Over the North China Plain and the Northeast China Plain, the model underestimates NH₃ columns by 62% on average, with a standard deviation of 45%, whereas over the Sichuan Basin, the underestimation reaches 65%, with a standard deviation of 30%. In contrast, the model generally overestimates NH₃ columns over the Indo-Gangetic Plain. Regarding spatial and temporal pattern of diurnal variations (Figs. 19–22), the largest discrepancies are observed in the areas of C1 in the Sichuan Basin and D1 in the Indo-Gangetic Plain, suggesting that the model has limited capability to simulate NH₃ in these areas and may require improvements through satellite-observed constraints to improve simulation accuracy.

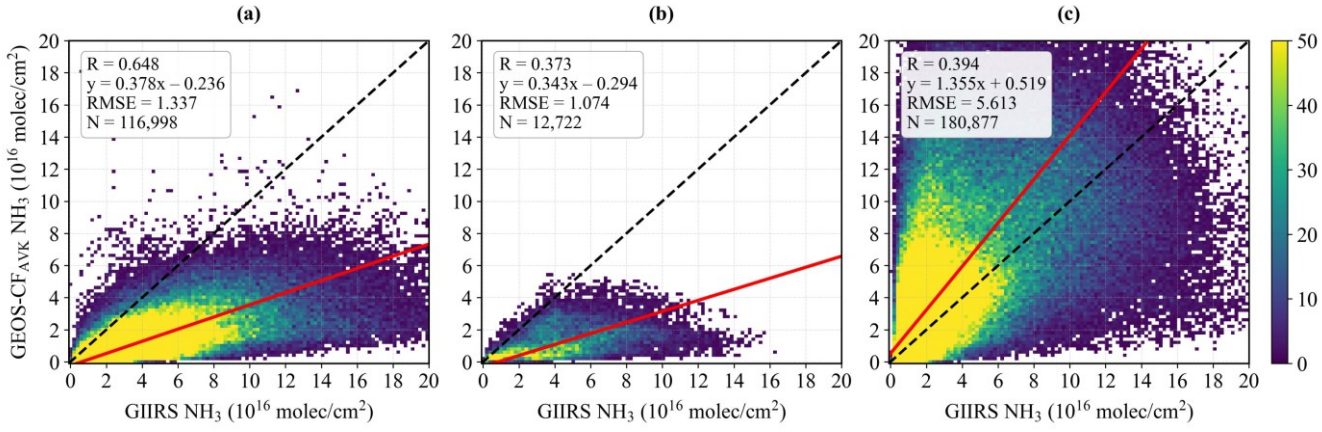


Figure 15. Comparison of NH₃ columns in May and June 2025 from GIIRS observations and GEOS-CF AVK-smoothed model simulations for (a) the North China Plain and the Northeast China Plain, (b) the Sichuan Basin, and (c) the Indo-Gangetic Plain. The model data is calculated by applying the AVKs from satellite retrievals to NH₃ profile (see Text S1).

4 Conclusions and Perspectives

The geostationary satellite observations from FY-4B/GIIRS provide a unique opportunity to monitor the diurnal variations of atmospheric NH₃ over East Asia, yet current research on this topic remains limited. In this study, we present a comprehensive analysis of three years of FY-4B/GIIRS observations from July 2022 to June 2025, revealing the spatiotemporal variations of NH₃ across East Asia and the distinctive daytime variations in agricultural emission regions.

NH₃ column concentrations from GIIRS observations exhibit pronounced local enhancements over major emission regions, particularly flat agricultural plains (e.g. the North China Plain, Northeast China Plain, the Indo-Gangetic Plain, the





Ningxia Irrigation Plain, the Wei River Plain, the Jianghan Plain, the Mekong Delta in Vietnam, the Chao Phraya River Plain in Thailand) with intensive crop cultivation and animal husbandry, and smaller-scale accumulation in topographically confined areas such as valleys and basins (e.g. the Sichuan Basin, oasis agriculture in the arid regions of Xinjiang in China, the Fergana Valley in Uzbekistan). After removing background levels derived from predefined reference regions, NH₃ enhancements show a consistent spatial pattern with anthropogenic emissions from the bottom-up MIX Asia emission inventory, and highlight these major emission source regions. The spatial distribution of NH₃ derived from GIIRS matches well with polar-orbiting satellite observations from IASI and CrIS.

The timing of peak NH₃ in the seasonal cycle primarily reflects agricultural activities related to fertilizer application, and is modulated by climatic factors such as temperature. For example, NH₃ columns generally exhibit a summer maximum (June-July) and a secondary spring maximum (April) in the North China Plain and Northeast China Plain. In southern regions of China, India, and Southeast Asia, NH₃ peaks during the late dry season (March-May) and declines sharply in the early wet season (June-July). Overall, regional differences in the timing of peak months follow a north-south gradient. Comparison with ground-based FTIR measurements and satellite-based IASI and CrIS observations show generally good agreement, yielding a correlation coefficient of 0.77 and an RMSE of 9.67×10¹⁵ molec/cm² relative to FTIR, while also consistently capturing the temporal variability of NH₃ columns.

This study reports the detailed daytime variations of NH₃ columns observed by FY-4B/GIIRS over the North China Plain, the Northeast China Plain, the Sichuan Basin, Hefei, and the Indo-Gangetic Plain. The NH₃ columns during the day generally increase from early morning to late afternoon, showing similar temporal variations to those observed by ground-based FTIR measurements at Hefei and simulated by GEOS-CF model in main agricultural source areas. Crucially, GIIRS provides substantial advantages by accurately characterizing spatial distributions and enabling continuous daily observations. GIIRS in the infrared is complementary to the Geostationary Environment Monitoring Spectrometer (GEMS; Kim et al., 2020), which operates in the ultraviolet/visible (UV/VIS) spectral range and provides hourly observations of trace gases such as NO₂ and SO₂ over East Asia. The synergy between GIIRS and GEMS enables joint investigations of NH₃ and NO₂, offering new opportunities to better quantify reactive nitrogen budgets and assess their impacts on air quality and climate. The planned launch of FY-4C/GIIRS in late 2025, together with FY-4B, will further enhance observational capabilities by providing broader spatial coverage and higher-frequency measurements. This emerging satellite constellation will offer unprecedented opportunities for monitoring diurnal cycles and emission processes across East and South Asia, thereby improving our understanding of atmospheric chemistry and supporting the development of more effective air pollution mitigation strategies.



537

538

539

540

541

542

543

544

545

546

547



536 Data availability.

The GIIRS NH₃ data (July 2022 to June 2025) used in this study is publicly available on Zenodo (https://doi.org/10.5281/zenodo.17193848). Further updates on the data will be provided on the project website (https://fengyunair.github.io/). The IASI L2 ammonia satellite observations are available from the AERIS data infrastructure (https://iasi.aeris-data.fr/, last access: 16 September 2025). The CrIS Fast Physical Retrieval (CFPR) ammonia dataset is Canada created by the Environment Climate Change and is publicly available (https://hpfx.collab.science.gc.ca/~mas001/satellite ext/cris/). The Hefei FTIR data are retrieved by Key Laboratory of Environmental Optics and Technology, Anhui Institute of Optics and Fine Mechanics, Chinese Academy of Sciences (Wang et al., 2022). The MIX emission inventory can be requested from the MEIC team (http://meicmodel.org.cn/?page id=2721). The GEOS-CF model data are available from High Performance Computing for Science, NASA Center for Climate Simulation (https://portal.nccs.nasa.gov/datashare/gmao/geos-cf/v1/das/Y2025/, last access: 10 August 2025).

Author contributions.

- MS and ZZ designed the study. MS carried out the result analysis and prepared the manuscript. ZZ and JH developed the GIIRS NH₃ retrieval algorithm. MS, RZ, SH, and SL collected and analyzed the emission sets. WW provided the FTIR data. RD, LZ, HC, ZC, and YG provided guidance on interpreting the satellite data and model simulations. ML provided guidance on analyzing emission inventory. NG, LC, MVD, and CC provided the IASI data and guided the interpretation. MWS provided the CrIS data and guidance. LL, CQ, FL, and CH provided guidance on analyzing GIIRS spectra. All authors reviewed and proofread the paper. LC is a senior research associate supported by the Belgian F.R.S.-FNRS.
- 554 Competing interests. The contact author has declared that none of the authors has any competing interests.
- Disclaimer. Publisher's note: Copernicus Publications remains neutral with regard to jurisdictional claims made in the text, published maps, institutional affiliations, or any other geographical representation in this paper. While Copernicus Publications makes every effort to include appropriate place names, the final responsibility lies with
- 558 the authors.
- Acknowledgements. We acknowledge the financial support of the National Satellite Meteorological Center (NSMC) of the China Meteorological Administration (CMA). We are grateful to the AERIS data infrastructure for providing access to the IASI NH₃ data. We thank the ECCC for making the CrIS NH₃ data publicly available. We



562

569



for Climate Simulation(NCCS) for sharing NH₃ data from GEOS-CF model simulations, and the ECMWF for sharing ERA-5 reanalysis data. This study was supported by the High-Performance Computing Platform of Peking University.

Financial support. This study was supported by the National Natural Science Foundation of China (No. 42275142), the China Postdoctoral Foundation (No. 2025M770242) and the National Key R&D Program of China (No. 2022YFA1003800).

also acknowledge the MEIC team for sharing the NH3 emission dataset from MIX inventory and the NASA Center





570 References

- 571 Beer, R., Shephard, M. W., Kulawik, S. S., Clough, S. A., Eldering, A., Bowman, K. W., Sander, S. P., Fisher, B. M., Payne,
- V. H., Luo, M., Osterman, G. B., and Worden, J. R.: First satellite observations of lower tropospheric ammonia and
- 573 methanol, Geophys. Res. Lett., 35, L09801, https://doi.org/10.1029/2008GL033642, 2008.
- 574 Behera, S. N., Sharma, M., Aneja, V. P., and Balasubramanian, R.: Ammonia in the atmosphere: a review on emission sources,
- atmospheric chemistry and deposition on terrestrial bodies, Environ. Sci. Pollut. Res., 20, 8092–8131,
- 576 https://doi.org/10.1007/s11356-013-2051-9, 2013.
- 577 Bobbink, R., Hicks, K., Galloway, J., Spranger, T., Alkemade, R., Ashmore, M., Bustamante, M., Cinderby, S., Davidson, E.,
- 578 Dentener, F., Emmett, B., Erisman, J.-W., Fenn, M., Gilliam, F., Nordin, A., Pardo, L., and De Vries, W.: Global
- assessment of nitrogen deposition effects on terrestrial plant diversity: A synthesis, Ecol. Appl., 20, 30-59,
- 580 https://doi.org/10.1890/08-1140.1, 2010.
- 581 Bowman, K. W.: TROPESS CrIS-JPSS1 L2 Ammonia for Forward Stream, Summary Product V1, Goddard Earth Sciences
- Data and Information Services Center (GES DISC), Greenbelt, MD, USA, available at:
- 583 https://doi.org/10.5067/2Q7XUY6OTKY1 (last access: 18 July 2025), 2022.
- Cady-Pereira, K. E., Guo, X., Wang, R., Leytem, A., Calkins, C., Berry, E., Sun, K., Müller, M., Wisthaler, A., Payne, V. H.,
- 585 Shephard, M. W., Zondlo, M. A., and Kantchev, V. H.: Validation of NH₃ observations from AIRS and CrIS against
- aircraft measurements from DISCOVER-AQ and a surface network in the Magic Valley, Atmos. Meas. Tech., 17, 15–
- 587 36, https://doi.org/10.5194/amt-17-15-2024, 2024.
- 588 Cady-Pereira, K., Payne, V., Bowman, K., Worden, J., Luo, M., Calkins, C., Kulawik, S., Whitten, K., and Fahy, K.:
- TROPESS-AIRS-CrIS NH3 Level 2 Product User Guide, Version 2.0, NASA Jet Propulsion Laboratory, Pasadena, CA,
- at: https://docserver.gesdisc.eosdis.nasa.gov/public/project/TROPESS/User Guides/TROPESS-AIRS-
- 591 CrIS NH₃ L2 Product User Guide 2-22-21.pdf (last access: 15 June 2024), 2021.
- 592 Cao, H., Henze, D. K., Shephard, M. W., Dammers, E., Cady-Pereira, K. E., Alvarado, M., Lonsdale, C., Luo, G., Yu, F., Zhu,
- L., Danielson, C. G., and Edgerton, E. S.: Inverse modeling of NH₃ sources using CrIS remote sensing measurements,
- 594 Environ. Res. Lett., 15, 104082, https://doi.org/10.1088/1748-9326/abb5cc, 2020.
- Chang, Y., Zou, Z., Zhang, Y., Deng, C., Hu, J., Shi, Z., Dore, A. J., and Collett, J. L. Jr.: Assessing contributions of agricultural
- and nonagricultural emissions to atmospheric ammonia in a Chinese megacity, Environ. Sci. Technol., 53, 1822–1833,
- 597 https://doi.org/10.1021/acs.est.8b05984, 2019.
- 598 Chen, F., Lao, Q., Li, Z., Chen, C., Zhou, X., and Zhang, S.: Monthly variations in the nitrogen isotope of ammonium in wet
- deposition in a tropical city of South China, Atmos. Chem. Phys., 20, 1062–1069,
- https://doi.org/10.4209/aaqr.2019.06.0303, 2020.
- 601 Chen, J., Du, X., Liu, X., Xu, W., and Krol, M.: Estimation of ammonia emissions over China using IASI satellite-derived
- surface observations, Environ. Sci. Technol., 59, 9991–10000, https://doi.org/10.1021/acs.est.4c10878, 2025.





- Chen, Y., Shen, H., Kaiser, J., Hu, Y., Capps, S. L., Zhao, S., Hakami, A., Shih, J.-S., Pavur, G. K., Turner, M. D., Henze, D.
- K., Resler, J., Nenes, A., Napelenok, S. L., Bash, J. O., Fahey, K. M., Carmichael, G. R., Chai, T., Clarisse, L., Coheur,
- P.-F., Van Damme, M., and Russell, A. G.: High-resolution hybrid inversion of IASI ammonia columns to constrain US
- ammonia emissions using the CMAQ adjoint model, Atmos. Chem. Phys., 21, 2067–2082, https://doi.org/10.5194/acp-
- 607 21-2067-2021, 2021.
- 608 Chen, Z.-L., Song, W., Hu, C.-C., Liu, X.-J., Chen, G.-Y., Walters, W. W., Michalski, G., Liu, C.-Q., Fowler, D., and Liu, X.-
- Y.: Significant contributions of combustion-related sources to ammonia emissions, Nat. Commun., 13, 7710,
- 610 https://doi.org/10.1038/s41467-022-35381-4, 2022.
- 611 Choi, H., Park, M. E., and Bae, J.-H.: Distinct regional and seasonal patterns of atmospheric NH₃ observed from satellite over
- East Asia, Remote Sens., 17, 2587, https://doi.org/10.3390/rs17152587, 2025.
- 613 Clarisse, L., Clerbaux, C., Dentener, F., Hurtmans, D., and Coheur, P.-F.: Global ammonia distribution derived from infrared
- 614 satellite observations, Nat. Geosci., 2, 479–483, https://doi.org/10.1038/ngeo551, 2009.
- 615 Clarisse, L., Shephard, M., Dentener, F., Hurtmans, D., CadyPereira, K., Karagulian, F., Van Damme, M., Clerbaux, C., and
- 616 Coheur, P.-F.: Satellite monitoring of ammonia: A case study of the San Joaquin Valley, J. Geophys. Res., 115, D13302,
- 617 https://doi.org/10.1029/2009JD013291, 2010.
- 618 Clarisse, L., Van Damme, M., Coheur, P.-F., and Clerbaux, C.: Tracking down global NH₃ point sources with wind-adjusted
- superresolution, Atmos. Meas. Tech., 12, 5457–5473, https://doi.org/10.5194/amt-12-5457-2019, 2019.
- 620 Clarisse, L., Van Damme, M., Hurtmans, D., Franco, B., Clerbaux, C., and Coheur, P.-F.: The diel cycle of NH₃ observed from
- the FY-4A Geostationary Interferometric Infrared Sounder (GIIRS), Geophys. Res. Lett., 48, e2021GL093010,
- https://doi.org/10.1029/2021GL093010, 2021.
- 623 Clarisse, L., Franco, B., Van Damme, M., Di Gioacchino, T., Hadji-Lazaro, J., Whitburn, S., Noppen, L., Hurtmans, D.,
- 624 Clerbaux, C., and Coheur, P.: The IASI NH₃ version 4 product: averaging kernels and improved consistency, Atmos.
- Meas. Tech., 16, 5009–5028, https://doi.org/10.5194/amt-16-5009-2023, 2023.
- 626 Clerbaux, C., Boynard, A., Clarisse, L., George, M., Hadji-Lazaro, J., Herbin, H., Hurtmans, D., Pommier, M., Razavi, A.,
- Turquety, S., Wespes, C., and Coheur, P.-F.: Monitoring of atmospheric composition using the thermal infrared
- 628 IASI/MetOp sounder, Atmos. Chem. Phys., 9, 6041–6054, https://doi.org/10.5194/acp-9-6041-2009, 2009.
- Dammers, E., Schaap, M., Haaima, M., Palm, M., Wichink Kruit, R. J., van Zanten, M. C., and Erisman, J. W.: Measuring
- atmospheric ammonia with remote sensing campaign: Part 1—characterisation of vertical ammonia concentration profile
- in the centre of The Netherlands, Atmos. Environ., 169, 97–112, https://doi.org/10.1016/j.atmosenv.2017.08.067, 2017a.
- Dammers, E., Shephard, M. W., Palm, M., Cady-Pereira, K., Capps, S., Lutsch, E., Strong, K., Hannigan, J. W., Ortega, I.,
- Toon, G. C., Stremme, W., Grutter, M., Jones, N., Smale, D., Siemons, J., Hrpcek, K., Tremblay, D., Schaap, M., Notholt,
- J., and Erisman, J. W.: Validation of the CrIS fast physical NH₃ retrieval with ground-based FTIR, Atmos. Meas. Tech.,
- 635 10, 2645–2667, https://doi.org/10.5194/amt-10-2645-2017, 2017b.





- Dammers, E., McLinden, C. A., Griffin, D., Shephard, M. W., Van Der Graaf, S., Lutsch, E., Schaap, M., Gainairu-Matz, Y.,
- Fioletov, V., Van Damme, M., Whitburn, S., Clarisse, L., Cady-Pereira, K., Clerbaux, C., Coheur, P. F., and Erisman, J.
- W.: NH₃ emissions from large point sources derived from CrIS and IASI satellite observations, Atmos. Chem. Phys., 19,
- 639 12261–12293, https://doi.org/10.5194/acp-19-12261-2019, 2019.
- Ding, Y., Ren, G., Li, Q., Sun, X., and Zhou, B.: High-impact extreme weather and climate events in China: summer 2024
- overview, Adv. Atmos. Sci., 41, 1123–1135, https://doi.org/10.1007/s00376-024-4462-6, 2024.
- 642 Gu, M., Pan, Y., Walters, W. W., Sun, Q., Song, L., Fang, Y., and Xue, Y.: Vehicular emissions enhanced ammonia
- concentrations in winter mornings: insights from diurnal nitrogen isotopic signatures, Environ. Sci. Technol., 56, 1578–
- 644 1585, https://doi.org/10.1021/acs.est.1c05884, 2022.
- 645 Guendouz, N., Viatte, C., Zeng, Z.-C., Boynard, A., Safieddine, S., Standfuss, C., Turquety, S., Van Damme, M., Clarisse, L.,
- 646 Coheur, P., Armante, R., Prunet, P., and Clerbaux, C.: Monitoring atmospheric ammonia from geostationary orbit:
- 647 contributions of GIIRS-B and IRS remote sensors, ESS Open Archive [preprint],
- https://doi.org/10.22541/essoar.175767134.49615241/v1, September 12, 2025.
- 649 Guo, X., Clarisse, L., Wang, R., Van Damme, M., Whitburn, S., Coheur, P.-F., Clerbaux, C., Franco, B., Pan, D., Golston, L.
- M., Wendt, L., Sun, K., Tao, L., Miller, D., Mikoviny, T., Müller, M., Wisthaler, A., Tevlin, A. G., Murphy, J. G., Nowak,
- J. B., Roscioli, J. R., Volkamer, R., Kille, N., Neuman, J. A., Eilerman, S. J., Crawford, J. H., Yacovitch, T. I., Barrick,
- J. D., Scarino, A. J., and Zondlo, M. A.: Validation of IASI satellite ammonia observations at the pixel scale using in-situ
- vertical profiles, J. Geophys. Res. Atmos., 126, e2020JD033475, https://doi.org/10.1029/2020JD033475, 2021.
- He, Y., Pan, Y., Zhang, G., Ji, D., Tian, S., Xu, X., Zhang, R., and Wang, Y.: Tracking ammonia morning peak, sources and
- transport with 1 Hz measurements at a rural site in North China Plain, Atmos. Environ., 235, 117630,
- https://doi.org/10.1016/j.atmosenv.2020.117630, 2020.
- Hersbach, H., Bell, B., Berrisford, P., Biavati, G., Horányi, A., Muñoz Sabater, J., Nicolas, J., Peubey, C., Radu, R., Rozum,
- I., Schepers, D., Simmons, A., Soci, C., Dee, D., and Thépaut, J-N.: ERA5 hourly data on single levels from 1940 to
- present. Copernicus Climate Change Service (C3S) Climate Data Store (CDS), https://doi.org/10.24381/cds.adbb2d47,
- 660 2023 (Accessed on 20-June-2025)
- Hou, X. and Yu, X.: An ammonia emissions inventory for agricultural sources in Hefei, China, Atmos. Ocean. Sci. Lett., 13
- 662 (3), 260–267, https://doi.org/10.1080/16742834.2020.1747355, 2020.
- Huy, D. H., Thanh, L. T., Hien, T. T., Takenaka, N., and Huy, D. H.: Characteristics of ammonia gas and fine particulate
- ammonium from two distinct urban areas: Osaka, Japan, and Ho Chi Minh City, Vietnam, Environ. Sci. Pollut. Res., 24,
- 8147–8163, https://doi.org/ 10.1007/s11356-017-8496-5, 2017.
- 666 Jang, J.-H., Hong, J., Kim, J. B., Park, S., Hwang, K., Kim, J., Kim, J. Y., Bae, G.-N., Kim, S., and Kim, K. H.: Influence of
- atmospheric ammonia on secondary inorganic aerosol formation in PM_{2.5} during spring 2024 in the Hongseong area,
- 668 Republic of Korea, Atmos. Environ., 358, 121363, https://doi.org/10.1016/j.atmosenv.2025.121363, 2025.





- 669 Keller, C.-A., Knowland, K.-E., Duncan, B.-N., Liu, J., Anderson, D.-C., Das, S., Lucchesi, R.-A., Lundgren, E.-W., Nicely,
- J.-M., Nielsen, E., Ott, L.-E., Saunders, E., Strode, S.-A., Wales, P.-A., Jacob, D.-J., and Pawson, S.: Description of the
- NASA GEOS composition forecast modeling system GEOS-CF v1.0, J. Adv. Model. Earth Syst., 13, e2020MS002413,
- https://doi.org/10.1029/2020MS002413, 2021.
- Kharol, S. K., Shephard, M. W., McLinden, C. A., Zhang, L., Sioris, C. E., O'Brien, J. M., Hakami, A., Murphy, J. G., van
- Donkelaar, A., and Martin, R. V.: Dry deposition of reactive nitrogen from satellite observations of ammonia and nitrogen
- dioxide over North America, Geophys. Res. Lett., 45, 1157–1166, https://doi.org/10.1002/2017GL076772, 2018.
- 676 Kim, J., Jeong, U., Ahn, M. H., Kim, J. H., Park, R. J., Lee, H., Song, C. H., Choi, Y. S., Lee, K. H., Yoo, J. M., Jeong, M. J.,
- Park, S. K., Lee, K. M., Song, C. K., Kim, S. W., Kim, Y. J., Kim, S. W., Kim, M., Go, S., Liu, X., Chance, K., Miller,
- 678 C. C., Al-Saadi, J., Veihelmann, B., Bhartia, P. K., Torres, O., Abad, G. G., Haffner, D. P., Ko, D. H., Lee, S. H., Woo,
- J. H., Chong, H., Park, S. S., Nicks, D., Choi, W. J., Moon, K. J., Cho, A., Yoon, J., Kim, S. kyun, Hong, H., Lee, K.,
- Lee, H., Lee, S., Choi, M., Veefkind, P., Levelt, P. F., Edwards, D. P., Kang, M., Eo, M., Bak, J., Baek, K., Kwon, H. A.,
- Kim, B. R., Shin, H. W., Choi, H., Lee, E., Chong, J., Cha, Y., Koo, J. H., Irie, H.,
- Hayashida, S., Kasai, Y., Kanaya, Y., Liu, C., Lin, J., Crawford, J. H., Carmichael, G. R., Newchurch, M. J., Lefer, B. L.,
- Herman, J. R., Swap, R. J., Lau, A. K. H., Kurosu, T. P., Jaross, G., Ahlers, B., Dobber, M., McElroy, C. T. and Choi, Y.:
- New era of air quality monitoring from space: Geostationary environment monitoring spectrometer (GEMS), B. Am.
- Meteorol. Soc., 101, E1–E22, https://doi.org/10.1175/BAMS-D-18-0013.1, 2020.
- Lan, Z., Lin, W., and Zhao, G.: Sources, variations, and effects on air quality of atmospheric ammonia, Curr. Pollut. Rep., 10,
- 687 40–53, https://doi.org/10.1007/s40726-023-00291-6, 2024.
- Li, M., Kurokawa, J., Zhang, Q., Woo, J.-H., Morikawa, T., Chatani, S., Lu, Z., Song, Y., Geng, G., Hu, H., Kim, J., Cooper,
- O. R., and McDonald, B. C.: MIXv2: a long-term mosaic emission inventory for Asia (2010–2017), Atmos. Chem. Phys.,
- 690 24, 3925–3952, https://doi.org/10.5194/acp-24-3925-2024, 2024.
- Lin, Y.-C., Zhang, Y.-L., Fan, M.-Y., and Bao, M.: Heterogeneous formation of particulate nitrate under ammonium-rich
- regimes during the high-PM_{2.5} events in Nanjing, China, Atmos. Chem. Phys., 20, 3999–4011
- https://doi.org/10.5194/acp-20-3999-2020, 2020.
- 694 Liu, L., Zhang, X., Wong, A. Y. H., Xu, W., Liu, X., Li, Y., Mi, H., Lu, X., Zhao, L., Wang, Z., Wu, X., and Wei, J.: Estimating
- 695 global surface ammonia concentrations inferred from satellite retrievals, Atmos. Chem. Phys., 19, 12051–12066,
- https://doi.org/10.5194/acp-19-12051-2019, 2019.
- Luo, X., Zhang, M., Ni, Y., and Shen, G.: Mitigation strategies for NH₃ and N₂O emissions in greenhouse agriculture: Insights
- into fertilizer management and nitrogen emission mechanisms, Environ. Technol. Innov., 37, 103995,
- https://doi.org/10.1016/j.eti.2024.103995, 2025.
- Marais, E. A., Pandey, A. K., Van Damme, M., Clarisse, L., Coheur, P.-F., Shephard, M. W., Cady-Pereira, K. E., Misselbrook,
- 701 T., Zhu, L., Luo, G., and Yu, F.: UK ammonia emissions estimated with satellite observations and GEOS-Chem, J.
- Geophys. Res. Atmos., 126, e2021JD035237, https://doi.org/10.1029/2021JD035237, 2021.





- Meng, Z. Y., Lin, W. L., Jiang, X. M., Yan, P., Wang, Y., Zhang, Y. M., Jia, X. F., and Yu, X. L.: Characteristics of atmospheric
- ammonia over Beijing, China, Atmos. Chem. Phys., 11, 6139–6151, https://doi.org/10.5194/acp-11-6139-2011, 2011.
- 705 Meng, Z., Xu, X., Lin, W., Ge, B., Xie, Y., Song, B., Jia, S., Zhang, R., Peng, W., Wang, Y., Cheng, H., Yang, W., and Zhao,
- H.: Role of ambient ammonia in particulate ammonium formation at a rural site in the North China Plain, Atmos. Chem.
- 707 Phys., 18, 167–184, https://doi.org/10.5194/acp-18-167-2018, 2018.
- Pai, S. J., Heald, C. L., and Murphy, J. G.: Exploring the global importance of atmospheric ammonia oxidation, ACS Earth
- 709 Space Chem., 5, 1674–1685, https://doi.org/10.1021/acsearthspacechem.1c00021, 2021.
- 710 Pawar, P. V., Ghude, S. D., Jena, C., Móring, A., Sutton, M. A., Kulkarni, S., Lal, D. M., Surendran, D., Van Damme, M.,
- 711 Clarisse, L., Coheur, P.-F., Liu, X., Govardhan, G., Xu, W., Jiang, J., and Adhya, T. K.: Analysis of atmospheric ammonia
- over South and East Asia based on the MOZART-4 model and its comparison with satellite and surface observations,
- 713 Atmos. Chem. Phys., 21, 6389–6409, https://doi.org/10.5194/acp-21-6389-2021, 2021.
- 714 Saraswati, G. M. P., Sharma, S. K., Mandal, T. K., Kotnala, R. K.: Simultaneous measurements of ambient NH₃ and its
- relationship with other trace gases, PM_{2.5} and meteorological parameters over Delhi, India, MAPAN, 34, 55–69,
- 716 https://doi.org/10.1007/s12647-018-0286-0, 2019.
- 717 Seinfeld, J. H. and Pandis, S. N.: Atmospheric chemistry and physics: from air pollution to climate change, 3rd edn., Wiley,
- 718 Hoboken, NJ, 1152 pp., ISBN 978-1-118-94740-1, 2016.
- 719 Shephard, M. W. and Cady-Pereira, K. E.: Cross-track Infrared Sounder (CrIS) satellite observations of tropospheric ammonia,
- 720 Atmos. Meas. Tech., 8, 1323–1336, https://doi.org/10.5194/amt-8-1323-2015, 2015.
- 721 Shephard, M. W., Dammers, E., Cady-Pereira, K. E., Kharol, S. K., Thompson, J., Gainariu-Matz, Y., Zhang, J., McLinden,
- 722 C. A., Kovachik, A., Moran, M., Bittman, S., Sioris, C. E., Griffin, D., Alvarado, M. J., Lonsdale, C., Savic-Jovcic, V.,
- and Zheng, Q.: Ammonia measurements from space with the Cross-track Infrared Sounder: characteristics and
- 724 applications, Atmos. Chem. Phys., 20, 2277–2302, https://doi.org/10.5194/acp-20-2277-2020, 2020.
- 725 Shephard, M. W., Kharol, S. K., Dammers, E., Sioris, C. E., Bell, A., Jansen, R., Caron, J., Snel, R., Palombo, E., Cady-Pereira,
- K. E., McLinden, C. A., Lutsch, E., and Knuteson, R.: Infrared satellite detection limits for monitoring atmospheric
- 727 ammonia, IEEE J. Sel. Top. Appl. Earth Obs. Remote Sens., 18, 10271–10291,
- 728 https://doi.org/10.1109/JSTARS.2025.3557240, 2025.
- 729 Teng, X., Hu, Q., Zhang, L., Qi, J., Shi, J., Xie, H., Gao, H., and Yao, X.: Identification of major sources of atmospheric NH₃
- in an urban environment in northern China during wintertime, Environ. Sci. Technol., 51, 6839-6848, https://doi.org/
- 731 10.1021/acs.est.7b00328, 2017.
- 732 Van Damme, M., Erisman, J. W., Clarisse, L., Dammers, E., Whitburn, S., Clerbaux, C., Dolman, A. J., and Coheur, P.-F.:
- Worldwide spatiotemporal atmospheric ammonia (NH₃) columns variability revealed by satellite, Geophys. Res. Lett.,
- 734 42, 8660–8668, https://doi.org/10.1002/2015GL065496, 2015.
- 735 Van Damme, M., Clarisse, L., Whitburn, S., Hadji-Lazaro, J., Hurtmans, D., Clerbaux, C., and Coheur, P.-F.: Industrial and
- 736 agricultural ammonia point sources exposed, Nature, 564, 99–103, https://doi.org/10.1038/s41586-018-0747-1, 2018.





- Van Damme, M., Clarisse, L., Franco, B., Sutton, M. A., Erisman, J. W., Wichink Kruit, R., van Zanten, M., Whitburn, S.,
- Hadji-Lazaro, J., and Hurtmans, D.: Global, regional and national trends of atmospheric ammonia derived from a decadal
- 739 (2008–2018) satellite record, Environ. Res. Lett., 16, 055017, https://doi.org/10.1088/1748-9326/abd5e0, 2021.
- 740 Wang, S., Nan, J., Shi, C., Fu, Q., Gao, S., Wang, D., Cui, H., Saiz-Lopez, A., and Zhou, B.: Atmospheric ammonia and its
- impacts on regional air quality over the megacity of Shanghai, China, Sci. Rep.-UK, 5, 15842,
- 742 https://doi.org/10.1038/srep15842, 2015.
- Wang, W., Tian, Y., Liu, C., Sun, Y., Liu, W., Xie, P., Liu, J., Xu, J., Morino, I., Velazco, V. A., Griffith, D. W. T., Notholt,
- J., and Warneke, T.: Investigating the performance of a greenhouse gas observatory in Hefei, China, Atmos. Meas. Tech.,
- 745 10, 2627-2643, https://doi.org/10.5194/amt-10-2627-2017, 2017.
- 746 Wang, W., Liu, C., Clarisse, L., Van Damme, M., Coheur, P.-F., Xie, Y., Shan, C., Hu, Q., Sun, Y., and Jones, N.: Ground-
- based measurements of atmospheric NH₃ by Fourier transform infrared spectrometry at Hefei and comparisons with IASI
- 748 data, Atmos. Environ., 287, 119256, https://doi.org/10.1016/j.atmosenv.2022.119256, 2022.
- 749 Warner, J. X., Wei, Z., Strow, L. L., Dickerson, R. R., and Nowak, J. B.: The global tropospheric ammonia distribution as seen
- 750 in the 13-year AIRS measurement record, Atmos. Chem. Phys., 16, 5467–5479, https://doi.org/10.5194/acp-16-5467-
- 751 2016, 2016.
- White, E., Shephard, M. W., Cady-Pereira, K. E., Kharol, S., Ford, S., Dammers, E., Chow, E., Thiessen, N., Tobin, D., Quinn,
- G., O'Brien, J., and Bash, J.: Accounting for non-detects in satellite retrievals: application using CrIS ammonia
- 754 observations, Remote Sens., 15, 2610, https://doi.org/10.3390/rs15102610, 2023.
- 755 Whitburn, S., Van Damme, M., Clarisse, L., Bauduin, S., Heald, C. L., Hadji-Lazaro, J., Hurtmans, D., Zondlo, M. A., Clerbaux,
- C., and Coheur, P.-F.: A flexible and robust neural network IASI-NH₃ retrieval algorithm, J. Geophys. Res.-Atmos., 121,
- 757 6581–6599, https://doi.org/10.1002/2016JD024828, 2016.
- Wunch, D., G. C. Toon, J.-F. L. Blavier, R. A. Washenfelder, J. Notholt, B. J. Connor, D. W. T. Griffith, V. Sherlock, and P.
- O. Wennberg: The Total Carbon Column Observing Network, Philos. Trans. R. Soc. A Math. Phys. Eng. Sci., 369(1943),
- 760 2087–2112, https://doi.org/10.1098/rsta.2010.0240, 2011.
- 761 Xu, J., Lu, M., Guo, Y., Zhang, L., Chen, Y., Liu, Z., Zhou, M., Lin, W., Pu, W., Ma, Z., Song, Y., Pan, Y., Liu, L., and Ji, D.:
- 762 Summertime urban ammonia emissions may be substantially underestimated in Beijing, China, Environ. Sci. Technol.,
- 763 57, 13124–13135, https://doi.org/10.1021/acs.est.3c05266, 2023.
- Yang, J., Zhang, Z., Wei, C., Lu, F., and Guo, Q.: Introducing the new generation of Chinese geostationary weather satellites,
- Fengyun-4B. Am. Meteorol. Soc., 98, 1637–1658, https://doi.org/10.1175/BAMS-D-16-0065.1, 2017.
- 766 Zeng, Z.-C., Lee, L., and Qi, C.: Diurnal carbon monoxide observed from a geostationary infrared hyperspectral sounder: first
- 767 result from GIIRS on board FengYun-4B, Atmos. Meas. Tech., 16, 3059–3083, https://doi.org/10.5194/amt-16-3059-
- 768 2023, 2023a.





- 769 Zeng, Z.-C., Lee, L., Qi, C., Clarisse, L., and Van Damme, M.: Optimal estimation retrieval of tropospheric ammonia from
- the Geostationary Interferometric Infrared Sounder on board FengYun-4B, Atmos. Meas. Tech., 16, 3693–3713,
- 771 https://doi.org/10.5194/amt-16-3693-2023, 2023b.
- 772 Zeng, Z.-C. FengYun-4B/GIIRS FYGeoAIR NH₃ retrievals from July 2022 to June 2025 [Data set]. Zenodo.
- 773 https://doi.org/10.5281/zenodo.17193848, 2025.
- Zhang, L., Chen, Y., Zhao, Y., Henze, D. K., Zhu, L., Song, Y., Paulot, F., Liu, X., Pan, Y., Lin, Y., and Huang, B.: Agricultural
- ammonia emissions in China: reconciling bottom-up and top-down estimates, Atmos. Chem. Phys., 18, 339–355,
- 776 https://doi.org/10.5194/acp-18-339-2018, 2018.
- 777 Zhou, X., Li, Y., Xiao, C., Chen, W., Mei, M., and Wang, G.: High-impact extreme weather and climate events in China:
- 778 summer 2024 overview, Adv. Atmos. Sci., 42, 1064–1076, https://doi.org/10.1007/s00376-024-4462-6, 2025.